NASA/TM-2008-215535

Measurement of Off-Body Velocity, Pressure, and Temperature in an Unseeded Supersonic Air Vortex by Stimulated Raman Scattering

Gregory C. Herring
Langley Research Center, Hampton, Virginia

October 2008

The NASA STI Program Office . . . in Profile

Since its founding, NASA has been dedicated to the advancement of aeronautics and space science. The NASA Scientific and Technical Information (STI) Program Office plays a key part in helping NASA maintain this important role.

The NASA STI Program Office is operated by Langley Research Center, the lead center for NASA’s scientific and technical information. The NASA STI Program Office provides access to the NASA STI Database, the largest collection of aeronautical and space science STI in the world. The Program Office is also NASA’s institutional mechanism for disseminating the results of its research and development activities. These results are published by NASA in the NASA STI Report Series, which includes the following report types:

- TECHNICAL PUBLICATION. Reports of completed research or a major significant phase of research that present the results of NASA programs and include extensive data or theoretical analysis. Includes compilations of significant scientific and technical data and information deemed to be of continuing reference value. NASA counterpart of peer-reviewed formal professional papers, but having less stringent limitations on manuscript length and extent of graphic presentations.
- TECHNICAL MEMORANDUM. Scientific and technical findings that are preliminary or of specialized interest, e.g., quick release reports, working papers, and bibliographies that contain minimal annotation. Does not contain extensive analysis.
- CONTRACTOR REPORT. Scientific and technical findings by NASA-sponsored contractors and grantees.
- CONFERENCE PUBLICATION. Collected papers from scientific and technical conferences, symposia, seminars, or other meetings sponsored or co-sponsored by NASA.
- SPECIAL PUBLICATION. Scientific, technical, or historical information from NASA programs, projects, and missions, often concerned with subjects having substantial public interest.
- TECHNICAL TRANSLATION. English-language translations of foreign scientific and technical material pertinent to NASA’s mission.

Specialized services that complement the STI Program Office’s diverse offerings include creating custom thesauri, building customized databases, organizing and publishing research results ... even providing videos.

For more information about the NASA STI Program Office, see the following:

- Access the NASA STI Program Home Page at ***http://www.sti.nasa.gov***
- E-mail your question via the Internet to help@sti.nasa.gov
- Fax your question to the NASA STI Help Desk at (301) 621-0134
- Phone the NASA STI Help Desk at (301) 621-0390
- Write to:
  NASA STI Help Desk
  NASA Center for AeroSpace Information
  7115 Standard Drive
  Hanover, MD 21076-1320

NASA/TM-2008-215535

Measurement of Off-Body Velocity, Pressure, and Temperature in an Unseeded Supersonic Air Vortex by Stimulated Raman Scattering

Gregory C. Herring
Langley Research Center, Hampton, Virginia

National Aeronautics and
Space Administration

Langley Research Center
Hampton, Virginia 23681-2199

October 2008

Available from:

NASA Center for AeroSpace Information (CASI)
7115 Standard Drive
Hanover, MD 21076-1320
(301) 621-0390

National Technical Information Service (NTIS)
5285 Port Royal Road
Springfield, VA 22161-2171
(703) 605-6000

Measurement of Off-Body Velocity, Pressure, and Temperature in an Unseeded Supersonic Air Vortex by Stimulated Raman Scattering

G. C. Herring

NASA Langley Research Center
Hampton, VA 23681-2199

Abstract

A noninvasive optical method is used to make time-averaged (30 sec) off-body measurements in a supersonic airflow. Seeding of tracer particles is not required. One spatial component of velocity, static pressure, and static temperature are measured with stimulated Raman scattering. The three flow parameters are determined simultaneously from a common sample volume (0.3 by 0.3 by 15 mm) using concurrent measurements of the forward and backward scattered line shapes of a N_2 vibrational Raman transition. The capability of this technique is illustrated with laboratory and large-scale wind tunnel testing that demonstrate 5-10% measurement uncertainties. Because the spatial resolution of the present work was improved to 1.5 cm (compared to 20 cm in previous work), it was possible to demonstrate a modest one-dimensional profiling of cross-flow velocity, pressure, and translational temperature through the low-density core of a stream-wise vortex (delta-wing model at Mach 2.8 in NASA Langley's Unitary Plan Wind Tunnel).

I. Introduction

Researchers have long realized that physical probes (e.g., Pitot probes and hot wires) can perturb the flow they are attempting to measure. Additionally, many hostile gases (flames, plasmas, and extreme hypersonic flow) are harmful to probes. Thus there has been a strong effort [1] at developing noninvasive diagnostics for flow measurement. Some methods seed small particles into the flow and determine velocity from the measured Doppler shift of Mie-scattered light. But Mie scattering gives no pressure and temperature information, and under some conditions [2, 3] the seed particles may not accurately follow the flow. Therefore methods that use light scattered directly from the molecular constituents of the flow are of interest. These molecular techniques do not require seeding of particles, and some work well in air, eliminating the need for trace gas seeding.

Many different techniques are being developed to measure fluid flow velocity, under the restriction of no seeding. Stimulated Rayleigh-Brillouin scattering [4], spontaneous Rayleigh scattering [5], Raman excitation plus laser-induced fluorescence [6], several other versions of laser-induced fluorescence [7-10], and laser-induced thermal acoustics [11] have all been experimentally demonstrated as viable approaches to velocimetry. Stimulated Raman methods (i.e., coherent) make up another category of optical diagnostics that can also be used to directly probe the N_2 or O_2 constituents of air.

Coherent anti-Stokes Raman scattering (CARS) is one well-known stimulated Raman technique, but it has historically measured only temperature. Velocity is an important flow parameter that is not easily measured by the spectrally-broadband CARS method, although one instance has been reported [12]. CARS is one of several related stimulated Raman methods [13, 14] that have been applied to gas measurement. Stimulated Raman gain spectroscopy (SRGS) is another and was chosen as the method for the present study - because of its capability for measuring velocity as well as temperature and pressure, and its ability to work at relatively low pressures, e.g., ~ 2 kPa (0.02 atm). In most stimulated Raman methods (including SRGS), two laser beams (frequencies separated by a molecular vibrational frequency) are crossed and overlapped in the flow. Molecules in the overlap region undergo Raman-based energy transitions and simultaneously emit four different coherent signals (see section II).

CARS is often used for temperature studies in harsh-environments, while SRGS is mostly restricted to basic studies of molecular parameters in benign laboratory environments. The CARS method uses rugged broadband lasers and provides a 10-nsec measurement time. Both characteristics contribute to its widespread use. In contrast, the time averaging necessary to obtain spectral line shapes and the delicate nature of the narrow-band lasers used in SRGS are drawbacks for real-world facility instrumentation. However, a significant advantage of SRGS is the inherent high-spectral resolution which provides the capability to measure velocity. Although difficult and expensive to implement, the SRGS approach for determining flow parameters has previously been demonstrated in laboratory [14-16] and large-scale wind-tunnel [17] environments.

The present work is an extension of previous work [17], which demonstrated that a SRGS apparatus could work in harsh wind-tunnel environments. The free-stream velocity measurements of Ref. 17 used collinear laser beams that gave a spatial resolution of only ≈ 20 cm. Here, new SRGS work is described in the Unitary Plan Wind Tunnel (UPWT) at NASA's Langley Research Center (LaRC). By crossing the input laser beams, an improved spatial resolution of 1.5 cm is achieved at the expense of reducing the signal by a factor of 10. Furthermore, additional signal is purposely sacrificed in order to partially simplify (as discussed in section II A) the relatively complicated laser apparatus of Ref. 17.

In this report, off-body, noninvasive, unseeded, spatially resolved, and time-averaged (30 sec), flow measurements in the vortex of a delta-wing model at Mach 2.8 are demonstrated with the simplified SRGS instrument, with improved spatial resolution. One-dimensional spatial profiles of cross-flow velocity, pressure, and translational temperature through the center of the vortex core are described. In addition, new laboratory work (collisional and Stark broadening of the line shape) is discussed to further illustrate the capability and limitations of SRGS as a flow diagnostic.

II. Quasi-cw Stimulated Raman Scattering

A. General Description

Spontaneous Raman scattering is summarized by a two-photon process in the energy level diagram of Fig. 1a and the experimental arrangement of Fig. 2. If a sample volume is irradiated with light at frequency ω_1, a spontaneous (i.e., incoherent) signal light at frequency ω_p is scattered nonuniformly over 4π steradians. Simultaneous with the light scattering, individual molecules are excited from the ground vibrational state, v = 0, to the first excited vibrational state, v = 1. Typical detection schemes collect only a small portion of this signal, at 90 deg relative to the input beam direction. Instrument (e.g., a spectrometer) and Doppler broadening of the line shape make velocity measurements from frequency-resolved Doppler shifts difficult. The spontaneous approach can be modified by adding a second laser beam to act as a seed signal at frequency ω_p that initiates the generation of stimulated (i.e., coherent or laser-like) Raman signal beams. The spectrometer is no longer necessary to isolate the signal light. The intensity of the stimulated Raman signal is much larger than the spontaneous signal, and the reduced instrument and Doppler broadening gives better frequency resolution for Doppler-based velocity measurements.

In these stimulated Raman methods, a gas medium is irradiated by two laser beams at frequencies ω_l and ω_p, where the subscripts "l" and "p" denote the pump and probe beams, respectively, and $\omega_l > \omega_p$. Two related and competing non-linear mechanisms occur simultaneously if the two frequencies are separated by a photon energy that corresponds to certain vibrational frequency differences Δ of the medium. One mechanism (Fig. 1b) is a two-photon process that generates two optical signals. Stimulated Raman gain spectroscopy (SRGS), is an optical gain signal induced on the ω_p laser beam and inverse Raman spectroscopy (IRS) is an attenuation (or absorption) signal induced on the ω_l laser beam. The second mechanism (Figs. 1c and 1d) is a four-photon process that generates two additional laser-like signal beams, CARS and coherent Stokes Raman spectroscopy (CSRS), where CSRS is pronounced as "scissors." The CARS signal is generated at a frequency $\omega_A = \omega_l + \Delta$, while the CSRS signal is generated at a frequency $\omega_S = \omega_p - \Delta$. In essence, two "input" laser beams enter the sample, and four laser beams emerge from the sample at four distinct wavelengths (all separated by frequency interval Δ) and in four distinct directions. The specific diagnostic that one utilizes depends on which signal laser beam one chooses to monitor. These four stimulated Raman techniques are summarized in the schematic of Fig. 3 and have been previously [13, 14] described in more detail. Both SRGS and IRS are sometimes [17] called Raman Doppler velocimetry (RDV), emphasizing the velocity capability of these two versions.

In principle, as a result of the quasi-cw stimulated Raman interaction with the gas, the energy-level populations and translational velocity distributions of the molecules are altered. In practice, the magnitude of the velocity change is small (~ 5 cm/sec worst case) and is negligible for bulk flow velocity of $\geq$ 5 m/sec. Also, the fraction of the molecules suffering velocity and internal energy modifications is small (few per cent or less) in the small-gain approximation that is valid for the conditions of the present work. Thus the perturbations to the flow are realistically negligible, and the techniques can essentially be called noninvasive.

The location of the measurement is defined by the overlap region at the crossing of the two input laser beams at ω_l and ω_p in Fig. 3. Because of phase-matching requirements, the CARS and CSRS beams are emitted from the measurement volume at different wavelengths and usually in different directions compared to the input beams. Thus these two signals are easy to isolate from unwanted stray light from the two input beams. In SRGS and IRS, the relatively small signals (gain and absorption) ride on top of the imperfectly steady input beams (acting as noisy backgrounds to the signals) and the temporal noise on the input beams strongly affects the signal-to-noise ratio (SNR). If velocity data is desired, then the choice between SRGS and IRS is usually dictated by whichever technique will give the best SNR. Typically, the absorption signal of IRS is generated on an argon-ion laser beam and the SRGS gain signal is generated on a tunable dye laser. IRS is usually superior, because the amplitude noise of the argon-ion laser is less than that of the tunable-dye-laser. Any continuous-wave (cw) Nd:YAG laser with low amplitude noise is also suitable for use in IRS.

Much previous work [15-17] has used the IRS version for optimum SNR, but at the expense of using a complicated five-laser instrument. In the work of this report, SNR is sacrificed on purpose, and the SRGS method is selected to obtain a relatively less expensive and less complex system – one which is relatively more user friendly in a large wind-tunnel environment. The SRGS system used in the present work requires only three lasers and one table full of optics - as opposed to the IRS system that requires five lasers and two tables full of optics. Although the SRGS system is significantly simpler and less costly compared to the IRS system, it remains relatively complicated and labor intensive relative to other techniques such as laser-based flow visualization, tunable diode laser spectroscopy, and traditional non-laser techniques (e.g., Schlieren).

Although the SRGS and IRS signal-beam powers are large compared to the CARS and CSRS signal powers, the SRGS and IRS signal powers are still small compared to the powers of the input beams (i.e., background) upon which they are superimposed. In SRGS, to separate the small gain signal from the background-input beam, the higher-frequency pump beam at ω_l is pulsed. The pulsed gain signal that is induced on the lower-frequency cw probe beam at ω_p is separated from the input probe beam by monitoring the beam power after it has emerged from the sample volume with an ac-coupled gated integrator. This particular version of SRGS is called quasi-cw stimulated Raman spectroscopy. In this approach, it is important that the temporal variations of the amplitude noise on the probe beam power be as small as possible. Amplitude noise levels of some potential probe lasers have been measured and compared [18].

B. Stimulated Raman Line Shape

The bulk flow and thermodynamic properties of the fluid are obtained from the line shape of the N_2 Raman transition that is driven by interaction with the input laser light. For Raman scattering near the forward direction of the pump beam, the net Doppler shift for the two-photon Raman process is minimal. Thus Doppler broadening of the Raman spectral line is relatively small and the forward Raman linewidth is determined mostly from pressure broadening and contains the pressure information. For scattering near the backward direction, net Doppler broadening is maximal and large compared to pressure broadening. Thus the backward Raman linewidth contains the Doppler-based translational temperature information. In general these Raman line shapes are Voigt profiles and the pressure and temperature information is determined from simultaneously fitting the forward and backward data to Voigt functions. The relative shift between the line centers of the forward and backward scattered light, governed by the Doppler shift of the bulk fluid movement, gives the velocity component in the direction of the beams. In the setup used in this work, both forward and backward Raman scattering from the same laser beams is observed simultaneously to obtain all of the above information as sketched in Fig. 4. Alternatively, the sequentially-obtained Doppler shifts in line centers between unknown moving and reference stationary gas samples also gives the same velocity information [15, 16].

In the approach outlined above, one varies the frequency difference between the two input laser beams to make a time-averaged (30-60 sec) measurement of the line shapes. This is accomplished by frequency tuning one of the input beams (e.g., cw probe at ω_p in this work) and recording the gain induced on this beam as a function of frequency difference. Under some flow conditions, the Raman transition widths (0.003 cm^{-1}) and line shifts (0.001 cm^{-1}) can be spectrally small, thus high-resolution lasers with narrow frequency bandwidths are necessary for this technique. It is relatively difficult to keep these narrow-band lasers properly operating, which leads to a significant level of effort for successful measurements even in a benign laboratory, let alone a harsh wind tunnel setting.

The magnitude of the SRGS signal power (i.e., the optical gain), in terms of the laser and gas parameters has been previously derived [13, 14]. Summarizing the results from Ref. 14 (in SI units), in the small-signal limit, the fractional change in total probe-laser beam power $\Delta P_p / P_p$, as a function of probe-laser angular frequency ω_p, is given by

$$\Delta P_p / P_p = \eta_2 \, G_2(\omega_p) \,, \qquad (1)$$

where η_2 and $G_2(\omega_p)$ are given by

$$\eta_2 = [2 / \pi] \arctan [\{f / r\} \tan \theta] \qquad (2)$$

and

$$G_2(\omega_p) = [4 \pi^2 / \varepsilon_o \, c \, \lambda_l \, \lambda_p] \, \chi''(\omega_p) \, P_l \,, \qquad (3)$$

where P_l is the incident pump-laser power and χ'' is the imaginary part of the third-order non-linear susceptibility which is a function of ω_p. Additionally λ_l and λ_p are the pump and probe laser wavelengths, c is the speed of light, ε_o is the free-space permittivity, f is the focal length of the lens that both focuses and crosses the pump and probe beams, θ is the full crossing angle, and r is the beam radius of the collimated beams on the focusing lens. If the frequency-dependent non-linear susceptibility is written in terms of the spontaneous differential Raman cross section, then $G_2(\omega_p)$ is written as

$$G_2(\omega_p) = [8 \pi^4 N \, c \, \omega_l \, \omega_p \, P_l / \{h \, [\omega_l - \Delta]^4\}] \, g(\omega_p) \, [d\sigma/d\Omega] \,, \qquad (4)$$

where h is Planck’s constant, N is the number density of molecules, Δ is the energy spacing between the upper and lower energy levels (2330 cm^{-1} for the case of the 0-1 vibrational transition in N_2), $d\sigma/d\Omega$ is the differential Raman cross section, and $g(\omega_p)$ is the area-normalized line shape function. In the special case where collisional broadening dominates the Raman line shape (e.g., pressure broadening dominates over Doppler broadening), $g(\omega_p)$ has a Lorentzian profile and is given by

$$g(\omega_p) = [\gamma / [2 \pi]] / [[\Delta - \omega]^2 + [\gamma / [2 \pi]]^2] \,, \qquad (5)$$

where γ is the full-width-half-maximum (FWHM) of the pressure-broadened line shape and ω is the absolute value of the difference $|\omega_l - \omega_p|$ between the pump and probe frequencies. In the special case where Doppler broadening dominates the Raman line shape, Eq. 5 takes the form of a Gaussian curve, $g(\omega_p) \propto \exp[- k \, (\Delta - \omega)^2]$, where k is a constant. In the general case where pressure and Doppler broadening contribute about equally to the line shape, Eq. 5 takes the form of a Voigt profile. The fluid flow parameters of velocity, pressure, and temperature are determined from fitting the Voigt version of Eq. 5 to the experimental Raman line shapes. The Gaussian and Lorentzian components provide the temperature and pressure respectively, while the line centers provide the Doppler shifts, which in turn provide bulk velocity.

Eqs. 4 and 5 show that the strength of the Raman signal is maximized when ω is zero (i.e., the pump and probe lasers are wavelength tuned such that $|\omega_l - \omega_p| = \Delta$) and that the maximum strength is proportional to the pump-laser power. In the quasi-cw experimental arrangement (i.e., the probe is cw and the pump is pulsed) of this work, the peak Raman signal, generated during the pump-pulse duration, is greatly increased relative to that of an equivalent pure-cw (i.e., both pump and probe laser are cw) arrangement. This increase of signal in a quasi-cw approach is typically obtained with a degradation of frequency (or velocity) resolution, since pulsed lasers generally have larger bandwidths than cw lasers.

The Δ in Eq. 5 is the Raman resonance frequency for still air. Thus Eq. 5 illustrates how the velocity of moving air can be measured. If the air is moving at velocity V, with respect to the lasers, then the resonance frequency Δ is Doppler shifted to a new value Δ' by

$$\Delta' = \Delta + \mathbf{V} \bullet \mathbf{dK}, \tag{5a}$$

where $\mathbf{V} \bullet \mathbf{dK}$ is the vector dot product of the flow velocity **V** and the wave vector difference **dK** between the pump and the probe laser beam wave vectors. Then resonance will not be observed at $\omega = \Delta$, but at $\omega = \Delta + \mathbf{V} \bullet \mathbf{dK}$. Thus bulk flow velocity is measured by observing the change in frequency of the Raman resonance without the need of an independent calibration. The velocity component measured is that along the vector **dK,** which is ≈ along the beam paths if the beams are crossed at a small angle ~ 1 deg or less.

III. Experimental Arrangement

A. Wind Tunnel Setup

The current work is oriented for applications in UPWT, a closed-circuit, supersonic air facility with a 1.2 by 1.2-meter test section. A top-view schematic of Fig.5a shows the final UPWT setup, where all depicted optical components are located outside of the test section. The delta wing, at 12 deg angle of attack (AOA) in a Mach 2.8 free-stream flow, generates two counter-rotating vortices in the flow field just above it. The crossing of three laser beams defines the sample volume, which is located in the right-hand vortex. Two laser beams, a cw 607-nm probe and a pulsed 532-nm pump, are incident transverse to the free-stream flow direction and cross at a small angle ($\theta = 0.5$ deg in Fig. 5) in the gas. A beam block stops the 532-nm beam, while the 607-nm beam is retro-reflected to cross the sample volume for a second time ($\theta = 0.5$ deg again) and monitored by a 0.5-ns risetime photodiode and gated integrators. This geometrical arrangement allows the simultaneous measurement of the forward and backward Raman line shapes.

The sample volume is defined by the mutual overlap of the three input-laser beams (pump, forward probe and backward probe) and is shaped like an elongated ellipsoid for a small crossing angle. Figs. 5c and 5d schematically show the size, shape and locations of typical measurement stations in relation to the delta wing for measurements on the right-side vortex. The focal length of the lenses in Fig. 5 is 120 cm. A collimated 1-cm diameter pump beam (532 nm) incident on the lens gives a beam diameter, at the focal point, of 150 µm. Allowing for beam crossing, the sample volume is about 1.5 cm (along the beam direction) by 300 µm (transverse to the beam axis). The value of 1.5 cm is estimated from the length of overlap region needed to generate 90% of the full signal. In this geometry, the spanwise velocity component of the vortex flow is measured, as described by Eq. 5a.

Two or three translation stages (with at least one located on each side of the test section) are used to translate the sample volume [19], while keeping the three input laser beams overlapped for near optimum Raman signal. In the schematic of Fig. 5b, a three-translation-stage version (three shaded elements) is shown with lenses L1, L2 and the retrometer mounted on three separate translators. This particular setup is used to translate the sample volume above the delta wing, over a line in the vertical direction with respect to the model. Fig. 5b is an upstream view with the free-stream flow directed out of the plane of the figure, towards the reader.

As the 607-nm laser is tuned over ~ 0.1 cm^{-1}, stimulated Raman scattering from a single rotational line of the N_2 vibrational Q-branch Raman transition is produced in both the forward and backward directions when the frequency difference ω of the two lasers matches the molecular resonance Δ. The forward signal propagates collinearly along the first 607-nm probe towards the retro-reflector, while the backward signal propagates collinearly along the second 607-nm probe towards the detector. Since the Q-switched 532-nm laser pulse (10-Hz repetition rate) limits the Raman interaction to 10-ns duration per pulse, the backward and forward Raman signals appear at the detector separated by a delay time (25 ns) defined by the separation between the sample volume and the retro-reflector.

Fig. 6 shows an example of the temporal profile obtained with the SRGS setup of Fig. 5 for the forward and backward Raman signals. The early small pulse is the backward signal, which is followed 25 nsec later by the later larger pulse, the forward scatter signal. The temporal location of four 10-nsec integrator gates are labeled. The earliest (1) and latest (4) occurring gates are used to record and subtract (post processing) the low-frequency fluctuation of the background level from the two Raman signals [gates (2) and (3)]. This broadband, low-frequency amplitude noise (~ 1 MHz) of the probe laser is not evident in the 200-nsec snapshot of Fig. 6, but would be obvious on longer time scales, and hinders the SNR. The background voltage from the first gate is subtracted from the backward signal voltage of gate 2 and the background from the last gate is subtracted from the forward signal of gate 3, for every laser shot. Alternatively, the forward signal could be subtracted form the backward signal, and then fit to a model of the difference of the forward and backward line shapes. This subtraction significantly improves the SNR for both the forward and backward signals by reducing the amplitude noise. Subtraction is necessary for reasonable SNR in low air densities, e.g. ~ 0.05 atm in the UPWT. Also shown in Fig. 6 is a high-frequency ~ 150-MHz noise that is RF radiation from the YAG laser Q-switch circuit.

Tuning over the Raman line shape requires 30-60 sec and allows the measurement of the absolute Raman linewidths and the line shift of the backward line relative to the forward line. The measured forward and backward Raman line shapes are fit [20] to a model of a Voigt [21] profile. The line shape model contains eight fitting parameters (the Lorentzian [pressure] and Gaussian [Doppler] components of the Raman transition and the background offset, peak height, and line center position for the both the forward and backward peaks). Both line shapes are fit simultaneously. The width of the forward line (~ 0.01 cm^{-1}) is dominated by pressure broadening and primarily determines static pressure, while the width of the backward line (~ 0.1 cm^{-1}) is dominated by Doppler broadening and primarily determines static translational temperature. The relative Doppler shift (~ 0.02 cm^{-1})

between the forward and backward lines determines the magnitude and direction of the bulk flow velocity parallel to the laser beams (i.e. the long dimension of the sample volume, which is transverse to the free-stream flow in the geometry of Fig. 5. Fig. 4 shows schematically how the various Raman line shape features relate to the flow sample parameters. If velocity is zero, both the backward and forward lines are centered on the unshifted location with different widths and peak heights.

B. Lasers

The setup described above uses two narrow-band, single longitudinal mode lasers. The first, the probe laser at λ_p = 607 nm, is a standing-wave cw dye laser that is pumped by an argon-ion laser. This dye laser produces about 150 mW of power with a time-averaged linewidth of 0.5 MHz. A small fraction of the dye laser output is diverted into a pair of temperature-stabilized etalons. The throughput of these two etalons is used to define the frequency axis each time that the dye laser is scanned over a Raman transition. The first etalon has a 150 MHz-free spectral range (FSR), and the second etalon has a 3-GHz FSR. Both etalons have a finesse of > 100. Typical etalon data, after normalizing to the power fluctuations of the laser, for a 6-GHz dye-laser scan is shown in Fig. 7. Typically the scan widths, determined separately from each etalon trace, agree to within 1 %. The errors in the measured velocities from scan-width uncertainties (and scan non-linearity) are negligible compared to the uncertainty resulting from low SNR of the measured Raman line shapes.

The second laser, the pump at λ_l = 532 nm, is a flashlamp-pumped, Q-switched, frequency doubled Nd:YAG laser that is seeded with a single-mode cw Nd:YAG laser, which is pumped with a diode laser in the near infrared. This laser produces about 150 mJ/pulse (10-nsec FWHM) at 10 Hz. The time-averaged linewidth (over one 30-sec dye-laser scan) is typically 70-100 MHz at 532 nm. This laser is monitored with a third temperature-stabilized etalon (FSR of 750 MHz and finesse of > 100) that is simultaneously scanned over the YAG laser spectral profile at the same time as the dye laser is scanned over the Raman signal. Thus the averaged YAG laser linewidth is recorded for each 30-sec dye-laser scan over the Raman transition. One example (FWHM = 90 MHz) of the Nd:YAG linewidth measured in the UPWT high-vibration environment is shown in Fig. 8.

For reference, the Fourier limit of the 10-nsec pulse is 45 MHz. When the YAG laser was new, a linewidth of 50-60 MHz could be routinely achieved in a typical laboratory environment. The extra linewidth of 70-100 MHz observed in the UPWT measurements is probably partly due to the advanced age of the laser during the tunnel testing and partly due to the vibrations in the UPWT test cell.

C. Laboratory Setup

Before the present work was initiated, the pressure broadening of the N_2 Raman transitions was well known at room temperature and above, but had not been measured below room temperature (100 K < T < 300 K), which was the expected temperature range of the supersonic gas in UPWT. Thus pressure broadening of the Raman line shape at temperatures below room temperature had to be quantified before the pressure could be determined from measured Raman line shapes of air in unknown wind tunnel conditions. Secondly, it was planned to use large laser powers to maximize the SRGS signals. Thus Stark broadening of the Raman line shape was measured to determine what laser power would be too large and corrupt the line-shape data through Stark broadening.

Only the forward Raman signal is necessary for both of these preliminary measurements for two reasons. First, pressure broadening is negligible in the Doppler-dominated backward scattering. Second, the forward linewidth is relatively small and shows Stark broadening before the broader backward linewidth. Both of these preliminary measurements were made in a preliminary SRGS laboratory setup, simpler than but somewhat similar to that of Fig. 5. There were three main differences between the final wind-tunnel setup of Fig. 5 and the preliminary laboratory setup. First, the retrometer of Fig. 5 was removed and only the forward-scattered SRGS signal was generated and detected. The detection scheme, including background subtraction, was the similar to that in Fig. 6. Another difference was that the translation stages were not used in this preliminary study, since no movement of the sample volume was necessary. Third, in place of the test section of the wind tunnel, a quartz gas cell (placed inside of an insulated refrigerator) was used so that the laser intensity, the N_2 gas temperature, and pressure could be controlled.

Before taking the instrument to the wind tunnel, the final SRGS setup of Fig. 5 was tested in the laboratory, including the addition of the retrometer, backward signal detection, and the translation apparatus to vertically move the sample volume. The quartz sample cell located at the beam-crossing region was retained to make Raman line shape measurements and to test the robustness of the optical alignment after vertical translation of the sample volume. Both the preliminary and the final setups used similar crossing angles and detection electronics as those used in the wind tunnel setup. One notable difference is that the preliminary forward-scatter-only Stark-broadening setup used shorter focal length lenses (to generate larger electric fields for the Stark-broadening characterization) than the 120-cm focal-length lenses that were used in the final UPWT setup of Fig. 5.

IV. <u>Results and Discussion</u>

A. Laboratory Results

In section A, five laboratory studies are described that were performed in support of the wind tunnel tests. A preliminary forward-scatter-only laboratory setup was used to study four issues, including the SRGS signal loss in the (A1) low-pressure limit. High-pump-laser-power limits, defined by (A2) gain narrowing or (A3) Stark broadening of the line shape, were also studied. Also, (A4) low-temperature pressure broadening coefficients were measured for use in analyzing unknown gas conditions at the cold temperatures expected in supersonic wind tunnels. In the fifth study, the final forward-backward UPWT apparatus was assembled to test (A5) the remote translation capability.

A1. Potential for Hypersonic Flow Measurement

Previous SRGS and IRS demonstrations have been with sonic or mild supersonic conditions and pressures of 1–100 kPa (0.01–1.0 atm or 7.6-760 Torr), where gas pressure primarily determines the forward Raman linewidth. At lower densities, the line shape is no longer dominated by pressure broadening and becomes constant for constant temperature. Then the strength of the forward Raman signal decreases with decreasing gas density. If the Raman linewidth γ is constant, Eq. 4 shows how the coherent Raman signal is linearly proportional to two factors: the gas density N and the pump laser power P_l.

This section presents a glimpse of the quality of forward-scatter data in the low pressure limit to indicate how SRGS would alternatively measure pressure (or density) – i.e. determination of signal strength at the low-pressures (0.1–1 kPa) typical of hypersonic flow. To be clear, this alternative method is different than the primary method for pressure measurement that is discussed in all other sections of this report. The gas is pure N_2, the temperature is 295 K, and only the forward Raman signal is used. The pump laser beam energy is increased to 145 mJ/pulse (14 MW peak power and peak intensity of ~ 100 GW/cm^2 for the pulsed 10-ns FWHM, 532-nm, ~ 150-μm-diameter focussed beams), and the crossing angle between the pump and the probe beams is 0.5 deg.

Fig. 9a shows two frequency scans over the J = 12 rotational transition (Q-branch) for different pressures. Peak signal strengths for these and other scans are plotted versus pressure in Fig 9b. The scans at 1 and 0.25 kPa are made with 330 laser pulses (33-sec average), but the scans near 0.1 kPa used 3300 pulses (5.5-min average). The good linearity of the signal with pressure (or density since temperature is constant) suggests that forward scatter SRGS could be used for averaged density measurements of air (or N_2) in the 10^{15}-10^{16} molecules/cm^3 regime. Potential hypersonic flow density measurements by this alternative method would be deduced from the peak signal strength and would require a calibration. This alternative method is different from the primary pressure measurement method described in later sections of this report. The results of Fig. 9b suggest the possibility of hypersonic applications at low pressures using SRGS with this alternative pressure (or density) measurement.

Henceforth, the alternative method of the above paragraph is ignored, and the remainder of this report includes only the primary pressure measurement method of pressure measurement by line shape analysis, as discussed in section II. This primary line-shape method does not require calibration. Since the Raman signal depends linearly on the pump laser pulse energy, one can increase the signal by increasing the laser pulse energy (i.e., peak power) as was done for the data of Fig. 9. However, two factors independently conspire to limit the amount of pump laser power that can be used without perturbing the measurements: gain narrowing and Stark broadening of the Raman line shape. Both of these perturbations will influence the linewidth and lead to poor-quality measurements. The next two sections address these issues.

A2. Gain Narrowing of the Stimulated Raman Line Shape

Gain narrowing is a non-linear process that occurs in coherent optical methods, but not in incoherent method like the spontaneous Raman process of Figs. 1a and 2. Gain narrowing [22] of the coherent Raman line shape occurs when the peak gain that is induced on the dc probe beam exceeds a few per cent of the dc probe power. This occurs when the pump beam intensity is significantly increased. The reason that the coherent Raman line shape is narrowed for large laser intensities is as follows. Eq. 1 gives the coherent Raman signal only in the small-signal limit approximation. A more general expression [13, 14, 23] for the signal (i.e., amplification of the Stokes power P_p^{input}) is

$$P_p^{output} / P_p^{input} \propto \exp\ [\text{line shape}]\ , \qquad (6)$$

where [line shape] is given by an expression identical to or similar to Eq. 5. As Refs. 13, 14, and 23 discuss, in the small-signal limit ($e^x \approx 1 + x$, if $x << 1$), Eq. 6 reduces to the approximation of Eq. 1, which can be alternatively written as

$$P_p^{output} - P_p^{input} = \Delta P_p / P_p \propto [\text{line shape}]\ . \qquad (7)$$

For common line shapes (e.g., Lorentzian, Gaussian, or Voigt), the non-linear function of Eq. 6 is narrower, in frequency domain, than the linear function of Eq. 7 (or Eq. 1) for a given temperature and pressure.

Thus large pump laser powers generate large Raman signals ($\Delta P_p / P_p \sim 1$ and Eq. 6 must be used) with narrower line profiles. In contrast, small pump powers generate small signals ($P_p^{output} / P_p^{input} << 1$ and the approximation of Eq. 7 is valid) with broader line profiles. This relatively narrow line shape of Eq. 6 is called “gain narrowing,” since this line profile is narrower than that expected from the linear situation of Eq. 7. Since large laser powers also generate artificial Stark broadening, signals acquired with large pump powers can exhibit line shapes with a complicated mixture of stark broadening and gain narrowing. Ideally, both of these perturbations to the Raman line shape should be avoided to maximize the accuracy with which pressure and temperature can be deduced.

In the ~ 0.1-kPa data of Fig. 9, gain narrowing is not a problem, since the density is so low that the peak signal level is, at maximum, only a few per cent of the dc probe laser value. However, at higher pressures ($\geq$ 10 kPa), with more Raman signal, gain narrowing could potentially corrupt the Raman line shape and spoil the pressure measurement by artificially narrowing the observed linewidth. At gas pressures of > 100 kPa (e.g., used in Raman shifting of laser beams) gain narrowing and collisional narrowing are more likely to occur. For all measurements presented in this report, gain narrowing has been mitigated by keeping the magnitude of the detected SRGS optical signals to about a few per cent of the dc probe laser level or less. This was confirmed with a series of laboratory measurements that will not be further described here.

A3. Stark Broadening of the Raman Line Shape

Generally, it is Stark broadening that determines the practical limit of useful laser power for the gas pressures common throughout this work. Stark broadening with electric fields that are uniform [24], that are defined by overlapped collinear Gaussian beams [25], and that are defined with crossed Gaussian beams [26] have been previously studied. In all three of these previous studies, it was shown that the Stark-broadened line shapes could be reasonably approximated with numerical simulations. In this section, the previous low-pressure work of Ref. 26, for crossed beam geometries, is complemented with additional results at higher-pressure. Successful simulations over an increased pressure range (the line shape changes significantly with pressure) provide additional confidence in the predictive ability of the numerical Stark-broadening model used here, or for future planning.

With zero applied electric field, the J^th rotational component of the Q-branch vibrational Raman transition consists of J + 1 orientational sub-components. These J + 1 transitions are degenerate: they overlap with each other in frequency domain and are indistinguishable. If an external electric field (e. g., a laser beam) is applied to a N_2 molecule, the J^th rotational component is broken up into J + 1 Stark sub-components. Each Stark sub-component has a line center slightly shifted from the unperturbed line center, and the magnitude of the shift depends on the strength of the electric field. In a non-uniform electric field (e.g., the focal region of a focussed laser beam), the varying electric field must be taken into account to accurately predict the Stark-perturbed line shape. In the quasi-cw SRGS approach taken here, the high-intensity pump laser generates the Stark broadening, while the low-intensity probe is negligible - it does not contribute to the Stark effect.

The model, used here, to predict Stark line shapes is the same as that of Refs. 25-27. The macroscopic sample volume (i.e. the crossing region of the two laser beams) is divided into a large number of microscopic volume elements ($V_{micro} << V_{sample}$) where the pump-laser intensity can be approximated as constant over a single microscopic element [27]. In addition, the 10-nsec Gaussian temporal profile is divided into many small time periods (t_{small} << 10 nsec) where the pump laser intensity can be approximated as constant over the time period t_{small}. The product of the pump and probe laser intensities determine how much Raman signal is generated from each microscopic 4-dimensional spatial-temporal element in the measurement process. Next the degree of Stark shift for each microscopic spatial-temporal volume element is calculated using the instantaneous pump-laser intensity (that produces the Stark broadening) and the Stark-shift coefficients [25] for each of the J + 1 orientational spectral components of the Stark-split Q-branch transition. The Raman line shape for each microscopic spatial-temporal element is generated by linearly summing all of the line shapes for each of the J + 1 components using known shift and weighting coefficients [25]. The final Raman line shape for the entire macroscopic sample volume is generated by linearly summing these line shapes over all the microscopic volume and temporal elements. In this final 4-dimensional summation, the product of pump and probe laser intensities (i.e., proportional to the Raman signal generated in each microscopic spatial-temporal volume element) is used as an additional weighting coefficient.

The numerical procedure used to generate the Stark-broadened line-shape R(ω) for a single rotational component J of the Q-branch vibrational Raman transition is constructed from a series of five nested summations over x, y, z, t, and M_j,

$$R(\omega) = \sum_{x} \sum_{y} \sum_{z} \sum_{t} \sum_{M_j = 0}^{J+1} W_1 \; W_2 \; V(\omega, \omega_o + \Delta\omega) \,, \qquad (8)$$

where x, y, z, are three Cartesian spatial coordinates with the z-axis collinear with the pump-beam axis, t is time, and M_j is the orientational quantum number associated with each of the J + 1 Stark sub-components. Thus R(ω) is a summation of many Voigt functions V(ω, ω_o+ Δω) with center frequencies ω_o shifted by frequency shift Δω. The Δω are

$$\Delta\omega = W_3(J, M_j)\ I(x, y, z, t)\ , \tag{9}$$

where the known Stark shifts per unit intensity $W_3(J, M_j)$ for each orientational sub-component have been previously tabulated in Ref. 25, and

$$I(x, y, z, t) = I_p\ \exp[-\ t^2 / t_o^2]\ \exp[-2\{x^2 + y^2\} / \{Z_p\ r_{op}^2\}] / [Z_p\ \Delta\omega_v] \tag{10}$$

is the approximately-constant laser intensity that induces the Stark shift in any one microscopic 4-dimensional volume element. The quantity $Z_p = 1 + \{z^2 / z_{op}^2\}$, I_p is the peak laser intensity (J/sec m^2) at the center of the focussed pump laser spot, and t_o is the laser temporal pulse width. The full width at half maximum of the Voigt line shape is $\Delta\omega_v$, while z_{op} and r_{op} are respectively the Rayleigh length and the spot size (1/e radius for electric field) for the pump laser beam.

The W_1 are weighting factors that give the relative strength of the individual orientational sub-components and are tabulated in Ref. 25. The W_2 are also weighting factors that give the relative amount of Raman signal generated in each particular microscopic volume element and depend on the strength of the electric field. Hence they are also functions of x, y, z, and t, and are given by

$$W_2 = \Delta x\ \Delta y\ \Delta z\ \ \exp[-\ t^2 / t_o^2]\ \exp[-2\{x^2 + y^2\} / \{r_{op}^2\ Z_p\}] \times$$

$$\exp[-2\{x_s^2 + y_s^2\} / \{r_{os}^2\ Z_s\}] / [Z_p\ \ Z_s\ \ \Delta\omega_v]\ , \tag{11}$$

where $Z_s = 1 + \{z_s^2 / z_{os}^2\}$, r_{os} is the spot size of the Stokes probe beam and z_{os} is the Rayleigh length for the Stokes beam. The volume of the individual microscopic elements is given by Δx Δy Δz. Finally, the Stokes-beam coordinates x_s, y_s, and z_s are related to the pump-beam coordinates x, y, and z by

$$\begin{aligned} x_s &= x \cos\theta - z \sin\theta\ , \\ y_s, &= y, \text{ and} \\ z_s &= z \cos\theta + x \sin\theta\ . \end{aligned} \tag{12}$$

Eq. 12 is the standard coordinate transformation for a simple rotation through angle θ in the x-z plane. The z_s axis is then collinear with the Stokes-probe-beam axis, where the z and z_s axes cross at angle θ.

This procedure previously showed good qualitative agreement with experiment [26] for low pressures (10 kPa). Furthermore, with collinear or crossed Gaussian beams and a seeded single longitudinal mode Nd:YAG laser, it was found that using one-half of the measured laser intensity gave good predictions for the low-pressure Stark-broadened Raman line shapes. In this section we show that this model (including the empirical factor of 0.5) also gives good agreement with experiment for higher-pressure conditions of 100 kPa.

Fig. 10a shows data and 10b shows the model for 100 kPa (i.e., 1 atm) of pure N_2 (J = 10) for two conditions: no-Stark broadening (peak intensity of 17 GW/cm^2) and Stark broadening with crossed (0.5 deg full angle) pump and probe beams. The Stark-broadened-case uses a measured peak pump-laser intensity of 700 GW/cm^2. Gain narrowing is avoided by keeping signal power small compared to the dc probe-laser power. The laboratory experimental setup described above was further modified to obtain the Stark-broadened (with collinear beams) and the no-Stark profiles simultaneously, as described in Ref. 26. Because of the low SNR and the small shifts of one line shape relative to the others, the measured collinear Stark case (i.e., Stark broadening with collinear pump and probe beams) is omitted to avoid cluttering the figure. The measured collinear Stark shift was observed to be about one half of the crossed case, and its location occurs right between the no-Stark case and the crossed-Stark case, i.e., the two line shapes of Fig. 10. To best fit the match between the simulation and the data, the peak laser intensity of the pump laser in the simulation of Fig. 10b was adjusted to 350 GW/cm^2 in the simulation (i.e., one-half of the 700 GW/cm^2 measurement).

This adjustment (smaller by a factor of two) of the laser intensity of the simulation at 100k Pa is the same as was required to find a good agreement between the model and the simulation for the low-pressure (10 kPa) work of Ref. 26. This consistent difference of a factor of two between the simulation and the data for both low and high pressure conditions shows that the laser beam parameters are constant and reproducible over long periods of time and for many alignments (since the disagreement is likely dependent on laser beam parameters, alignment, and their measurement). The disagreement of a factor of two in laser intensity is actually not bad, considering the uncertainties associated with measuring the laser intensity of ~ 10^3 GW/cm^2 in a focussed beam and the imperfections in the Gaussian beams for both the spatial and temporal profiles. Thus the discrepancy (a factor of two) is considered as agreement, and the consistency of the factor of two (for different pressures, beam geometry's, and individual alignments) demonstrates the ability to reproduce the Stark-related experimental conditions.

This agreement to within a factor of two, between the simulated and the measured line shapes, at both small [26] and large (Fig. 10 of this work) pressures, provides confidence that Stark broadening can be reliably predicted over a wide range of gas pressures, including the range expected in the UPWT. Based on the work of this section and Ref. 26, a pump-laser pulse energy of 40 mJ/pulse (peak intensity of 20 GW/cm^2) was selected as a compromise to simultaneously maximize the SRGS signal and minimize Stark broadening. During the UPWT testing, a pump energy of 80 mJ/pulse was briefly tried (as a test) and no extra linewidth was observed. Thus Stark related errors are expected to be small (compared to other errors), since all of the UPWT results reported here are with the 40mJ/pulse.

A4. Measurement of Pressure Broadening Below 300 K

Pressure broadening of the Q-branch (0-1) vibrational transition in N_2 has been widely studied (see citation list in Refs. 28 and 29) because of the importance of combustion temperature measurements by the CARS technique. However nearly all studies were limited to the temperature regime above 300 K because combustion temperatures are > 300 K. Since temperatures of 100–300 K were expected in the non-reacting supersonic airflow of the present work, pressure broadening in this lower-temperature regime had to be independently measured before unknown data from wind tunnels could be analyzed. A low-temperature pressure broadening study was completed [28] before performing the UPWT measurements, and provided pressure broadening results down to about 100 K.

In the present study, an empirical equation was created (based on data of Ref. 28) to predict the pressure broadening coefficient (PBC) over the temperature regime 100–300 K, for several rotational components of the Raman Q-branch transitions. This equation is used in the non-linear fitting routine that determines pressure from the line shapes and is

$$\mathrm{PBC} = \mathrm{PBC}_o\,[298 / T]^A, \qquad (13)$$

where the PBC_o are the room temperature pressure broadening coefficients and T is the temperature in Kelvin. Room temperature values PBC_o can be found in Ref. 29. In the current work, the exponent A is given by

$$A = 0.4 + 0.38\,\{64 / [64 + (J - 8)^2 + 2\,(J - 8)]\}, \qquad (14)$$

where J = the rotational quantum number of the Q-branch rotational component. Fig. 11 shows a comparison of Eq. 13 and the measurements of Ref. 28 and 29. Eqs. 13 and 14 are empirical approximations and slightly disagree (see Fig. 11) with the measurements of Ref. 28. But because of the low SNR of the wind tunnel data to be presented in section IV B2, the uncertainties in the SRGS pressure measurements will be dominated by the low SNR of the line shape and not by the approximate nature of Eqs. 13 and 14.

Eq. 14 was generated to obtain a formula to work for low-J transitions, modest SNR, and temperatures $\leq$ 300 K. For future SRGS data with extremely good SNR, the exact measured values of the coefficients from Ref. 28 should be used. For temperatures well above 300 K, the models given in the high-temperature studies in the citation list of Ref. 28 should be used. Eqs. 13 and 14 should be used only for moderate SNR or worse, for temperatures $T \approx 100$–300 K, and for transitions $J \approx 0$–20.

In section IV B1, free-stream results from the UPWT will be presented. These include gas pressure measurements (at low temperatures) made using SRGS and the pressure broadening coefficients of Ref. 28. In that section the reader will see that the SRGS pressure measurements are in good agreement with the pressure and temperature expected in the test section (determined by standard wind tunnel instrumentation). However, there is an alternative viewpoint with which to interpret the pressure data of section IV B1. If one considers the supersonic flow as a gas sample with known pressure and temperature, then the data acquired in the wind tunnel represents an independent study of the low-temperature pressure broadening of N_2 Raman transitions in air. This is a reasonable viewpoint since the UPWT is a long-used, well-characterized supersonic tunnel [30]. The SRGS pressure data that are presented in section IV B1 can be re-analyzed by not letting temperature vary and fixing the temperature to the known free-stream value. Then one is independently verifying the low-temperature pressure broadening measurements of Ref. 28 when fitting the wind tunnel data to determine gas pressure.

The re-analyzed results of some randomly-selected wind tunnel runs of section IV B1 are shown in Fig. 12 for $J = 6$. Different temperatures are obtained during different Mach number runs. The good agreement of the pressure determined from the SRGS data line-shape fits at UPWT (with fixed temperatures and pressure broadening coefficients from Ref. 28) and the known tunnel pressure (from traditional probes) constitutes an independent experimental confirmation of the low-temperature pressure broadening measurements of Ref. 28. Thus the data, above 2 kPa, of Fig. 12 are in quantitative agreement with the results of Ref. 28, to within the combined uncertainties of the two SRGS studies, and confirms the earlier work. The uncertainties of the expected UPWT values are negligible compared to the SRGS uncertainties. The three lowest data points, around 1-1.5 kPa are expected to show worse agreement because the fitted Raman linewidths are approaching the instrument resolution (indicated by the vertical arrow labeled "equivalent laser linewidth") and the SRGS uncertainties of these three points are increasing as pressure decreases.

Although Ref. 28 reports pressure broadening by pure N_2 and the results of Fig. 12 are for broadening by air, the difference is minimal. The magnitude of the foreign-gas broadening of O_2 is close to the self broadening of N_2. Thus the difference between air and pure N_2 broadening is ~ 1%, less than the combined uncertainty of the two studies.

A5. Laboratory Demonstration of SRGS Instrument

Before the SRGS instrument was used at UPWT, the full forward-backward setup (as shown in Fig. 5) was set up in a laboratory and tested on gas samples with known conditions. These laboratory measurements are not a calibration of the SRGS instrument (which does not require a calibration as discussed in section II B), but simply verify correct operation of the instrument. Pure N_2, in a cell, laboratory room air, and air in the partially evacuated test section at UPWT were used as stationary gas samples. The full 8-parameter fitting routine, as described in section III A, was used to determine air speed, pressure, and translational temperature. Fig. 13 shows an example of a single 30-sec measurement of the Raman forward and backward line shapes for room air (295 K and 100 kPa). The slight disagreement between the data (jagged curves) and the fits (smooth curves) on the right side is because the line-shape model simply sums-over-the Js. For the example of $J = 6$ in Fig. 13, the nearest neighbors ($J = 4$, 5, 7, and 8) are added to $J = 6$ to get the line-shape wings of $J = 6$ correct at the relatively high pressure of 100 kPa (1 atm). However, it is well known [29] that one must use a nonlinear collisional-narrowing model to get the best agreement with overlapping rotational lines. A computationally more expensive collisional-narrowing line shape model would better account for a reduction in pressure broadening due to closely spaced (and overlapping) lines. However, all of the measurements made in the low-pressure conditions of UPWT are free from this small error, because the nearest J neighbors do not overlap at low ($\leq$ 10 kPa) pressures. Thus the simple sum-over-the-J model used here is more than adequate for the present UPWT work.

Fig. 14 shows the simultaneously measured velocity, pressure, and temperature on a static gas, for a series of single 30-sec measurements, in the laboratory cell (left side) and at UPWT (right side) with no flow in the test section. The SRGS-determined pressures are compared to Baratrons for the laboratory data and the standard UPWT instrumentation for the no-flow UPWT data. The solid diagonal line in the pressure plot represents perfect agreement between SRGS and the known conditions. SRGS temperatures are compared to thermocouples (TC) for room temperature, and velocities are compared to zero for the stationary gas. After calibration by standard procedures, the laboratory TC was further checked with liquid-N_2 and H_2O-ice baths, and the laboratory Baratron was checked with an independent pressure meter. The differences in the two methods are dominated by the errors in the SRGS method, not by the Baratron or TC measurements.

The only point that is averaged over more than one 30-sec scan is the single pressure point with an error bar, which shows the average of the eight UPWT points (all at the same pressure) and the 68% confidence level (standard deviation = $\pm$ 1 σ) of the sample. A nonrigorous estimate of the SRGS uncertainties for the single-scan measurements of Fig. 14 can be made from the numerical uncertainties as determined from the non-linear line-shape fitting algorithm. However, a better estimate of the SRGS uncertainties can be determined by comparing the SRGS-derived values to the expected or known gas parameter values. Calculating the root-mean-square (rms) of the differences between the measurements and known conditions provides one estimate of uncertainty for each of the three parameters. These uncertainties include random (i.e., precision) and systematic (i.e., accuracy) contributions. For pressure, the rms difference is $\pm$ 1.0 kPa, for temperature it is $\pm$ 17 K, and for the combined velocity set (UPWT plus laboratory) it is $\pm$ 13 m/s. The purely random component of the velocity error (i.e. $\pm$ 1 σ) for each of the two velocity sets are shown with the means in the top plot.

In these tests, it was also demonstrated that the Raman sample volume could be translated 20-30 cm in one dimension (using either two or three translators) without losing the optical alignment. After the best initial alignments, not more that about 10% of the Raman signal was lost (due to misalignment of the three Raman input beams at the focal point) after translation of the sample volume over 20–30 cm in room air. Results of Fig. 14 show that the full-translating instrument is working adequately, with SRGS derived parameters in agreement with the known gas conditions. Although the alignment of the system in Fig. 5 is straightforward, it is also tedious. It is also easily disrupted due to environmental vibrations or inevitable changes in of any one of the input laser beam pointing directions. The alignment typically has to be updated several times a day.

B. Unitary Plan Wind Tunnel (UPWT) Results

Here, new SRGS measurements made in the 1.2 by 1.2 by 2.1-meter test section of the UPWT [30] at LaRC are described for supersonic free-stream conditions and in the flow of a delta wing. As discussed in the introduction, two trade offs were made to sacrifice signal for the practical considerations of improved spatial resolution and a simplification of the instrument (compared to Ref. 17). The model was a delta wing with a leading-edge sweep angle of 75-deg and a trailing-edge span of 30.5 cm. The leading edges were sharp with a 10-deg bevel. The AOA was 12-deg and the Mach number was 2.8 (630 m/sec). Nominal free-stream pressures and temperatures are 3.3 kPa (0.033 atm) and 127 K, with both quantities further decreasing inside the vortex core.

Crossing the Raman laser beams ($\theta = \pm$ 0.5 deg), as in Figs. 5a, generates a highly ellipsoidal-shaped sample volume with a long spanwise dimension of 1.5 cm. The streamwise and vertical dimensions were about 300 μm. This highly elongated sample volume is schematically indicated in Fig. 5c for eight vertical locations above the delta wing. Crossing the beams significantly improves upon previous non-crossed-beam RDV work [17] in UPWT that obtained only 20-cm resolution in free-stream measurements. Estimates of both of these spatial resolutions were obtained from numerical simulation [27] of the generation of stimulated Raman signal.

Reduction of the spanwise spatial resolution from 20 to 1.5 cm allowed the possibility for rough profiling of the flow parameters through the core of one of the vortices that are generated above the lifting delta wing model. The sample point of the current work is translated relative to the model by translating a portion of the optical system, not including the lasers, as shown in Fig. 5b. Data at different vertical locations through the core of the vortex are acquired sequentially. Only the one velocity component is measured in the configuration used here.

B1. Free-Stream Measurements

To provide an additional check (not a calibration) of the SRGS instrument, measurements were made in the free-stream where the flow conditions were known. Since the beams are crossed at a small angle of 1 deg in Fig. 5a, the instrument is oriented to measure the cross-flow velocity component of the vortex, and the measured free-stream velocity component will be the spanwise component (i.e., ≈ zero). Negative signs for velocity indicate flow away from the lasers, while positive signs indicate flow towards the lasers. To make free-stream measurements, the delta wing model was moved downstream of the sample volume. Fig. 15 shows sample experimental Raman line shapes and the associated fits for a single 30-sec free-stream measurement. Fig. 16 contains the first main result of this work and shows reasonable agreement between the SRGS-derived velocity, pressure, and temperature and the known wind tunnel test conditions for a series of averaged free-stream measurements, where each average is over three to eight 30-sec scans (taken in ≤ 20 min). The 1 σ error bars show a few selected standard deviations of the sample for the averaged points. The spatial resolution of the data of Fig. 16 is about 1.5 cm, an improvement of ≈ 20 times over Ref. 17.

For pressure and temperature, an estimate of the total uncertainties (systematic plus random) of the SRGS measurements can be made by using the flow parameters supplied by the standard UPWT instrumentation as the true value. The rms values of the differences between the SRGS and the expected wind-tunnel values give uncertainties of ± 0.4 kPa for pressure (ignoring the two points below the laser equivalent width) and ± 14 K for temperature. The total uncertainty in velocity is conservatively estimated from the spread in the measured rms deviations about the expected velocity of zero and is, ± 14 m/s for all 14 measurements on days 1 and 2. These velocity and temperature free-stream uncertainties are the same as the laboratory uncertainties of Fig. 14, while these pressure uncertainties are one half of the laboratory uncertainties. Generally the uncertainty estimates from the laboratory data of Fig. 14 are consistent with the free-steam uncertainties of Fig. 16.

Two comments concerning systematic errors in the velocity measurements are in order. Offsets of ≈ -10 and +10 m/sec are seen for Days 1and 2 (separated by a vertical line), in the free-stream measurements of Fig. 16. The direction of the velocity component measured is purposely pointed downstream, about 1.3 deg off from the exact spanwise direction (because of a combination of the SRGS beam geometry and an effort to minimize optical back reflections exactly into the lasers). This angle $\gamma \approx 1.3$ deg has been accounted for in plotting the velocity data in Fig. 16. However, any error in the measurement of this 1.3-deg angle will generate a systematic error in the final velocity measurement. A conservative estimate of the total error in the measurement direction is ≈ 0.5 deg (due to slight realignments of the SRGS instrument throughout a typical work day) and this corresponds to a velocity error of about ± 6 m/s. In addition, the true spanwise velocity in the free-stream flow may be slightly different from zero (see Ref. 30). An uncertainty of ± 3 m/sec is estimated from the summed contribution of streamwise Mach number and spanwise flow angle uncertainties. Adding the SRGS and the flow uncertainty contributions in quadrature gives a final uncertainty of about ± 7 m/sec, roughly consistent with the ± 10 m/sec offsets seen in Fig. 16.

Simple estimates of the precision-only uncertainties are made with the 68% confidence levels (± 1σ of the sample), for repeated measurements. These estimates are about ± 8 m/sec, and are consistent with the no-flow data in Fig. 14. The uncertainties of the means (± 4 m/sec) are about one half of the uncertainties of the samples, since the number of measurements in each sample is 3-8. Clearly, Day 2 has a larger random error – possibly the laser noise is larger than typical or the tunnel vibration was worse on this day.

In summary, velocity uncertainties can be estimated with three different methods are as follows. The purely random error is about ± 5 m/sec (see Day 1 Fig. 16). The total error (random plus systematic) is about ± 10 m/sec from the offsets of the averages from zero (for stationary gas), or a second estimate for the total error is from the rms deviations of about ± 13 m/sec (Figs. 14 and 16).

B2. Delta-Wing Vortex Measurements

This section presents the results of a proof-of-concept demonstration of a spatially resolved flow measurement near a model of interest in a large-scale wind tunnel. The goal was to generate a linear map of spanwise velocity, pressure, and temperature through the core of a vortex. Although the spanwise resolution of 1.5 cm in still somewhat large compared to the dimensions of the flow gradients, it is small enough to capture the course structure of the vortex. The important novel aspect of these measurements is the nonintrusive nature of the SRGS technique on the vortex.

A five-hole Pitot probe had previously been used to map the vortices as part of an unrelated project (unpublished). That same probe was used as a guide for positioning the present Raman sample point in the vortex. Fig. 17 shows forward (Fig. 17a) and backward (Fig. 17b) SRGS line shapes from single 30-sec measurement after the background subtraction was performed. The raw SNR of the measurements in the vortex were the smallest of any measurements presented in this report. The Raman spectral lines of Fig. 17 are not observable until the background subtraction is performed. This low SNR is due to the low gas densities, and subtraction is imperative for the vortex data.

Fig. 18 shows a series of eight 30-sec single-scan measurements for velocity, pressure, and temperature. They were made at one fixed location within the vortex, 2 cm from the vortex center and 4 cm above the wing surface. The stream-wise location of these measurements is 25 mm upstream of the delta-wing trailing edge. The velocity, pressure, and temperature at each time were made simultaneously, and are related to each other. The nonrigorous 68% confidence levels ($\pm 1\sigma$) for a single point (i.e., a single 30-sec scan) are estimated from the nonlinear fits and are typically ± 30 m/sec, ± 0.5 kPa, and ± 30 K. The variation over 70 min shows the combined effect of uncertainties in the Raman measurements and any possible long-term time variation of the flow. Means and 1σ of the means are shown in the figure. 1σ of the sample of eight measurements is $\sqrt{8}$ larger.

Fig. 19 contains the second main result of the present work and shows two profiles of spanwise velocity, pressure, and temperature through the core of one of the two vortices as shown in Fig. 5a. Each of the three panels in the figure shows two 1-dimensional maps (filled diamonds and open squares) in the vertical direction, at a stream-wise position that is 25 mm upstream of the trailing edge of the delta wing. Each of the 1-d maps required about 2 hours of tunnel run time. Each data point is the average of ≈ six 30-sec measurements, and required ≈ 15 min to acquire. The data at the different spatial locations was acquired sequentially; however at any one location, the velocity, pressure, and temperature were acquired simultaneously. The vertical location of each measurement is specified on the abscissa as the distance above the delta wing surface.

Considering the diamond data of Fig. 19, the velocity data show a direction reversal at a location 28 mm above the wing. Negative velocities indicate flow away from the lasers in Fig. 5a and flow towards the right-hand side of Fig. 5c. The temperature and pressure are both minimum at ≈ 24 mm, and both increase as the measurement point is moved in either direction, towards or away from the surface. Increases in temperature and pressure at the position nearest the surface, accompanied by a decrease in velocity, occur as the flow is heated and slowed in the boundary layer. The measured profile generally illustrates the expected qualitative features of a vortex. Any deviations of this SRGS data from more accurate attributes of a vortex [31, 32] may be due to the spatial averaging over 1.5 cm of spanwise distance for the measurement volume (see Fig. 5c). For Fig. 19, the 68% confidence levels (based on 1σ of the mean) are ± 10 m/s for velocity, ± 0.1 kPa for pressure, and ± 10 K for temperature. Uncertainties for 1σ of the samples increase by $\sqrt{6}$.

The diamonds of Fig 19 were acquired after the five-hole probe (used for alignment) was backed far downstream from the trailing edge and measurement location. The squares of Fig. 19 show a second vertical scan (same free-stream run conditions) made on another day at the same heights, except 4 mm upstream of the diamond measurement. The filled diamond and open square data of Fig. 19 were acquired at measurement stations denoted by the filled and open circles, respectively shown in Fig. 5d. In addition for this second measurement (i.e., open squares), the Pitot probe was not backed downstream of the SRGS measurement location after it was used for the initial alginment. However, it was far enough removed from each of the SRGS measurement stations so that the bow shock of the probe was not influencing the data. Thus the second difference between the diamond and square data of Fig. 19 is the stream-wise location of the Pitot probe.

Note three unusual aspects of the two SRGS data sets. The square data of Fig. 19 show less pronounced changes (versus vertical location) in all three parameters, compared to the diamond data. Second, not only do the two SRGS profiles disagree with each other, but the expected vortex center line (dashed line determined from a Pitot probe survey completed before the SRGS test) disagrees with each of the two SRGS profile centers (i.e, velocity = zero). Third, for each SRGS profile, the location of velocity reversal (i.e, velocity = zero) is slightly offset from the location of minimum pressure and temperature. For example, in the diamond data, the SRGS-measured velocity reversal is at about 2.8 cm above the surface, while the pressure and temperature minimums are both at 2.4 cm. The dashed line at 1.7 cm indicates the expected center line of the vortex from the probe survey.

A likely cause for second and third aspects of the data is the geometry of the measurement as shown in Fig. 5a. The axis of the vortex is tilted off from the tunnel centerline by about $\beta \approx 4$ deg [31], which has not been accounted for in the data of Fig. 19. Since the free-stream velocity = 630 m/sec, then one expects a velocity offset of - 630 sin (4 deg) = - 44 m/sec (along the SRGS measuring direction away from the lasers). Thus the position of velocity reversal in Fig. 19 may be too far from the surface compared to the view if the angle $\beta = 0$. If the filled diamond data of Fig. 19 were to be corrected (increased 44 m/sec) for this expected offset, then the velocity profile would be more symmetrically centered around zero and the location of velocity reversal would move from 2.8 to 2.3 cm (matching the pressure and temperature minimum at 2.4 cm to within the spatial resolution and missing the expected center from the probe survey by only 5mm instead of the11 mm illustrated in Fig. 19).

A possible cause for the first aspect (the difference in the two SRGS measurements) is that the presence of the nearby pressure probe has moved the transverse position of the vortex relative to the model. This could obviously explain the difference between the square data (probe tip left at the trailing edge during SRGS measurements) and the diamond data (probe tip moved far downstream from the trailing edge during SRGS measurements) and plausibly explain the residual difference (≈ 5mm) between the diamond SRGS measurements and the expected centerline (dashed line) from the probe survey. Thus the SRGS measurements (squares) of Fig. 19 are possibly showing a perturbation of the vortex due to the presence of the nearby Pitot probe. The difference in streamwise location of

4mm for the square measurement (compared to the diamond measurement) is not nearly enough streamwise location change to explain the obvious difference in shape for the two profiles of Fig. 19.

The interpretation of probe perturbation of the vortex is supported by crude flow-visualization work that was performed during the same time period as the SRGS work. Nonintrusive Rayleigh scattering of the pump laser beam at 532 nm (with naked-eye detection) was used to visualize [33] one-dimensional tracks of gas density through the vortices of the delta wing model. The experiment of Ref. 33 showed that the presence or absence of the nearby probe seemed to influence the relative transverse position of the visualized vortex, consistent with the results of Fig. 19. This flow visualization was done without addition of water to the flow. This interpretation is similar to observations by other researchers. A subsonic study [34] also reported a transverse movement of the vortex core, under rare conditions (e.g., when a probe is very near the vortex core axis) due to the presence of a 7-hole pressure probe. However, Ref 34 does report excellent agreement between the probe and Laser Doppler Velocimeter (LDV)-based vortex maps.

A third possible explanation for the difference in the two SRGS measurements is that the SRGS measurement volume was inadvertently moved relative to the model for the two runs. Thus the measurement volume would also move relative to the vortex center, giving the relatively straighter velocity profile of the squares, compared to the exaggerated "S" profile of the diamonds (presumably through the vortex center). However, the same alignment procedure was used for each of the two measurements, where the Pitot probe was used a reference point to set the Raman sample volume location. The positioning of the probe is easily reproducible to ~ 1 mm from day to day. This explanation of imperfect positioning of the SRGS sample volume is certainly possible, but unlikely.

A comment on Figs. 14, 16, 18, and 19 may be useful. Temperature is typically determined with a larger uncertainty than pressure, because the SNR is less for the backward data (which determines temperature) than the forward data. The uncertainty in the temperature typically limits the uncertainty in pressure and velocity. Velocity is limited by the uncertainty in the determination of the line center for the backward line shape. Since pressure depends (see Eq. 13) on the PBC, and the PBC is approximately $\propto T^{0.6}$, then imperfectly determined temperatures cause additional errors in the pressure. This latter effect is easily seen in plots (not shown) of pressure errors as a function of temperature errors. A clear correlation exists between the pressure and temperature errors. The fractional pressure error is typically larger than the fractional temperature error and is also approximately linearly proportional to the temperature error.

C. Future Improvements

The primary impediment to optimum SNR in the present measurements is floor vibration in the UPWT test cell environment. This facility vibration is transmitted to the optical table and slightly vibrates the probe beam on the detector active area, creating excess amplitude noise on the 607-nm probe-laser intensity. Thus the raw spectra, from which these results are derived, have SNR that are significantly smaller than the largest possible SNR that is determined by the usual amplitude noise of the cw dye laser beam. Flow facilities with milder vibration environments, than encountered at UPWT facility at LaRC, would clearly allow smaller measurement uncertainties than those quoted in this work.

If facility vibration is negligible, then the usual amplitude noise (from dye-jet fluctuations) on the cw-dye laser [18] dominates the uncertainty. Other lasers have smaller amplitude noise than the dye laser used here. Replacing the relatively simpler three-laser setup of SRGS that was used here, with the more costly and complicated five-laser IRS setup, would allow the use of a laser (e.g., argon-ion or solid state Nd:YAG) with smaller amplitude noise. This would provide another reduction in the measurement uncertainties compared to those reported here. However, extra effort and labor are necessary to operate the IRS system. In spite of the additional cost and complexity, it is recommended that the IRS technique be used to achieve the smallest possible uncertainties in future work (in cases where facility vibration is not an issue). Another reason for this recommendation is that the residual complexity of the simplified SRGS system continues to require a moderate degree of tedious alignment.

V. Summary

This report describes a noninvasive and unseeded optical technique, stimulated Raman gain spectroscopy (SRGS), that simultaneously measures off-body velocity, temperature, and pressure in supersonic air. It is based on stimulated Raman scattering from a single rotational line of the vibrational Q-branch transitions in the N_2 molecule. Comparison of the SRGS-derived flow parameters with expected tunnel values from known free-stream conditions shows good agreement and provides estimates of the SRGS uncertainties.

Spatially resolved (~ 1 cm) and time-averaged (~ 30 sec) measurements of velocity, temperature, and pressure in the free stream and in a vortex over a lifting delta-wing model are demonstrated in a large-scale supersonic tunnel. One-dimensional profiles of the three flow parameters through the vortex core are presented. Noninvasive SRGS measurements, with and without a 5-hole Pitot probe positioned near the SRGS measurement station, may illustrate a possible perturbation of the vortex due to the presence of the nearby probe.

Laboratory work is also presented that illustrates the accuracy and limitations of quantitative measurements at gas conditions of 100-300 K and 1-10 kPa (0.01–0.1 atm). These laboratory measurements show the potential for future hypersonic work at pressures of 0.1 kPa, as well as limitations of the technique due to Stark line shape broadening and hi-gain induced line-shape narrowing.

VI. Acknowledgements

I thank J. E. Byrd, P. F. Covell, M. E. Hillard, Jr., W. R. Lempert, B. W. South, I. J. Walker (Lockheed Engineering and Sciences), and the UPWT staff (especially R. L. Hall) for contributions to this work.

VII. References

1. A. C. Eckbreth, *Laser Diagnostics for Combustion Temperature and Species*, (Abacus Press, Cambridge MA, 1988).

2. R. H. Nichols, "Calculation of Particle Dynamics Effects on Laser Velocimeter Data," NASA Conference Publication 2393, pgs. 1-11 (1985).

3. W. A. Hunter, Jr., L. R. Gartrell, W. M. Humphreys, Jr., D. W. Witte, and C. E. Nichols, "Development and Assessment of an LDV System for Mach 6 Flow Field Measurements," *New Trends in Instrumentation for Hypersonic Research*, ed. By A. Boutier, 337-346 (1993).

4. G. C. Herring, H. Moosmüller, S. A. Lee, and C. Y. She, "Flow Velocity Measurements with Stimulated Rayleigh-Brillouin-Gain Spectroscopy," Opt. Lett. **8**, 602-604 (1983).

5. R. G. Seasholtz and J. Panda, "Rayleigh Scattering Diagnostic for Dynamic Measurement of Velocity and Temperature," paper AIAA-99-0641, 37th Aerospace Sciences Meeting, Reno, NV (11-14 January1999).

6. R. Miles and W. Lempert, "Two-Dimensional Measurement of Density, Velocity, and Temperature in Turbulent High-Speed Air Flows by UV Rayleigh Scattering," Appl. Phys. B **51**, 1-7 (1990).

7. M. Allen, et. al., "Velocity Field Imaging in Supersonic Reacting Flows Near Atmospheric Pressure," AIAA Journal **32**, 1676-1682 (1994).

8. R. W. Pitz, et. al., "Unseeded Velocity Measurement by Ozone Tagging Velocimetry," Opt. Lett. **21**, 755-757 (1996).

9. N. M. Sijtsema, N. J. Dam, R. J. H. Klein-Douwel, and J. J. ter Meulen, "Air Photolysis and Recombination Tracking: A New Molecular Tagging Velocimetry Technique," AIAA Journal **40**, 1061-1069 (2002).

10. L. Boedeker, "Velocity Measurement by H_2O Photolysis and Laser-Induced Fluorescence of OH," Opt. Lett. **14**, 473-475 (1989).

11. R. C. Hart, G. C. Herring, and R. J. Balla, "Common-Path Heterodyne Laser-Induced Thermal Acoustics for Seedless Velocimetry," Opt. Lett. **27**, 710-712 (2002).

12. M. Lefebvre, B. Scherrer, P. Bouchardy, and T. Pot, "Transient Grating Induced by Single-Shot Time-Domain Coherent Anti-Stokes Raman Scattering: Application to Velocity Measurements in Supersonic Flows," J. Opt. Soc. Am. B **13**, 514-520 (1996).

13. M. D. Levenson, *Introduction to Nonlinear Laser Spectroscopy*, (Academic Press, New York, NY, 1982); also see “Coherent Raman Spectroscopy,” Phys. Today, (May 1977).

14. C. Y. She, H. Moosmüllller, and G. C. Herring, “Coherent Light Scattering for Supersonic Flow Measurements” Appl. Phys. B **46**, 283-297 (1988).

15. H. Moosmüller, G. C. Herring, and C. Y. She, "Two-Component Velocity Measurement in a Supersonic Jet with Spatially Resolved Inverse Raman Spectroscopy," Opt. Lett. **9**, 536-538 (1984).

16. G. C. Herring, S. A. Lee, & C. Y. She, "Measurements of a Supersonic Velocity in a Nitrogen Flow Using Inverse Raman Spectroscopy," Opt. Lett. **8**, 214-217 (1983).

17. R. J. Exton and M. E. Hillard, “Raman Doppler Velocimetry: A Unified Approach for Measuring Molecular Flow Velocity, Temperature, and Pressure,” Appl. Opt. **25**, 14-21 (1986).

18. G. C. Herring and M. E. Hillard, Jr., “Noise Amplitude Measurements of Single-Mode CW Lasers at Radio Frequencies,” IEEE J. Quantum Electron. **28**, 570-572 (1992).

19. G. C. Herring and B. W. South, and R. J. Exton, “Apparatus Translates Crossed-Laser-Beam Probe Volume,” NASA Tech Briefs **18**, 41-42 (1994).

20. P. R. Bevington, *Data Reduction and Error Analysis for the Physical Sciences*, p. 235, McGraw-Hill, New York (1969).

21. A. K. Hui, B. H. Armstrong, and A. A. Wray, “Rapid Computation of the Voigt and Complex Error Functions,” J. Quant. Spectrosc. Radiat. Transfer **19**, 509-516 (1978).

22. J. T. Verdeyen, *Laser Electronics,* pgs. 155, 182 (Prentice-Hall Inc., Inglewood Cliffs, New Jersey, 1981).

23. A. Owyoung, “Coherent Raman Gain Spectroscopy Using CW Laser Sources,” IEEE J. Quantum Electron. **QE-14**, 192-203 (1977).

24. L. A. Rahn, R. L. Farrow, M. L. Koszykowski, and P. L. Mattern, “Observation of an Optical Stark Effect on Vibrational and Rotational Transitions,” Phys. Rev. Lett. **45**, 620-623 (1980).

25. H. Moosmüllller, C. Y. She, and W. M. Huo, “Optical Stark Effects in the Four-Wave Mixing and Stimulated Raman Spectra of N_2,” Phys. Rev. A **40**, 6983-6998 (1989).

26. G. C. Herring and M. E. Hillard, Jr., “Stark Broadening Using Crossed Gaussian Beams in Stimulated Raman Spectroscopy,” J. Quant. Spectrosc. Radiat. Transfer **57**, 739-744 (1997).

27. G. C. Herring and M. E. Hillard, Jr., “Effect of Crossed Beams on Stokes Gain and Interaction Length in Stimulated Raman Gain Spectroscopy,” Appl Opt. **34**, 6837-6841 (1995).

28. G. C. Herring and B. W. South, “Pressure Broadening of Vibrational Raman Lines in N_2 at Temperatures Below 300 K,” J. Quant. Spectrosc. Radiat. Transfer **52**, 835-840 (1994).

29. G. J. Rosasco, W. Lempert, W. S. Hurst, and A. Fein, “Line Interference Effects in the Vibrational Q-branch Spectra of N_2 and CO,” Chem. Phys. Lett. **97**, 435-440 (1983).

30. C. M. Jackson, Jr., W. A. Corlett, and W. J. Monta, “Description and Calibration of the Langley Unitary Plan Wind Tunnel,” NASA TP-1905 (November 1981).

31. S. N. McMillin, J. L. Thomas, and E. M. Murman, “Navier-Stokes and Euler Solutions for Lee-Side Flows Over Supersonic Delta Wings,” NASA TP-3035 (December 1990).

32. S. R. Donohoe, E. M. Houtman, and W. J. Bannich, “System for the Study of Vortex Breakdown Over a Delta Wing,” paper AIAA 94-2480, 18th Aerospace Ground Testing Conference, Colorado Springs, CO (June 20-23 1994).

33. G. C. Herring and M. E. Hillard, Jr., “Flow Visualization by Elastic Light Scattering in the Boundary Layer of a Supersonic Flow,” NASA TM-2000-210121, pg. 9 (August 2000).

34. J. T. Kegelman and J. F. Roos, “The Flowfields of Bursting Vortices Over Moderately Swept Delta Wings,” paper AIAA-90-0599, 28th Aerospace Sciences Meeting, Reno, NV (8-11 January1990).

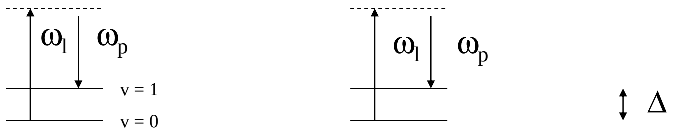

(a) Spontaneous (b) SRGS and IRS

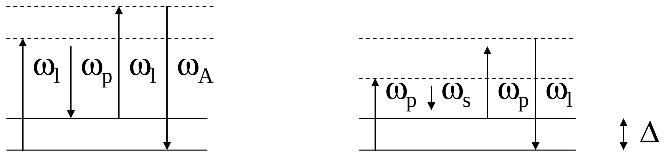

(c) CARS (d) CSRS

Fig. 1 Energy level diagram for spontaneous and four stimulated Raman spectroscopies.

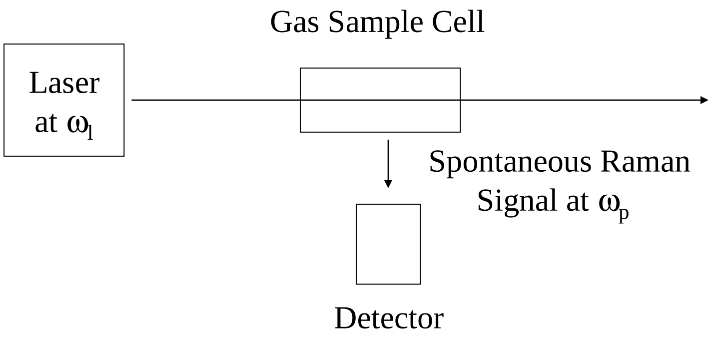

Fig. 2 Schematic experimental arrangement for traditional spontaneous Raman spectroscopy.

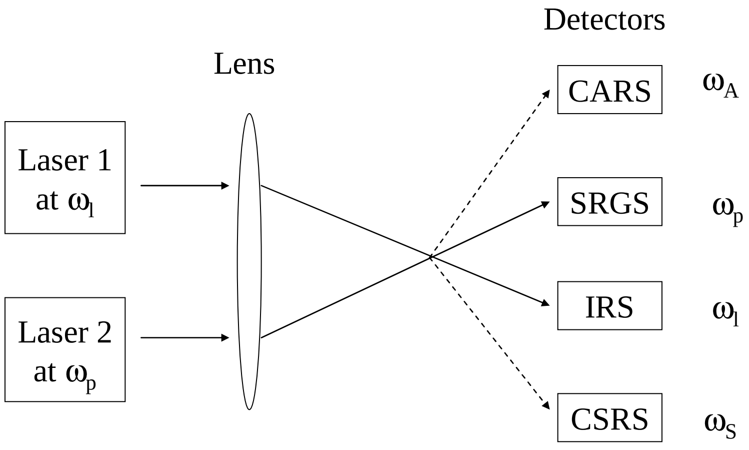

Fig. 3 Schematic arrangements for four stimulated Raman spectroscopies.

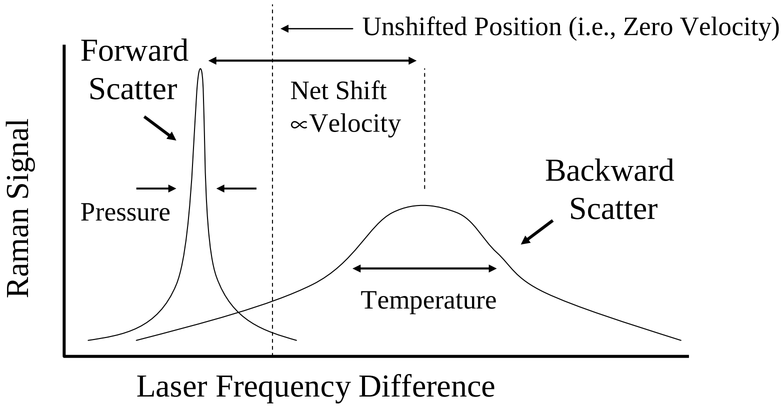

Fig. 4 Principle of the SRGS technique for the measurement for velocity, pressure, and temperature from forward and backward Raman line shapes.

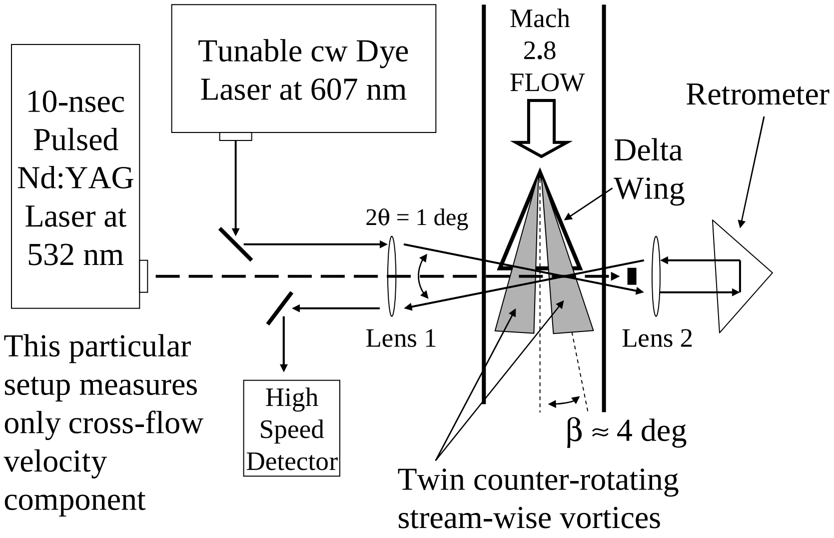

Fig. 5a Top-view schematics of SRGS apparatus at the UPWT.

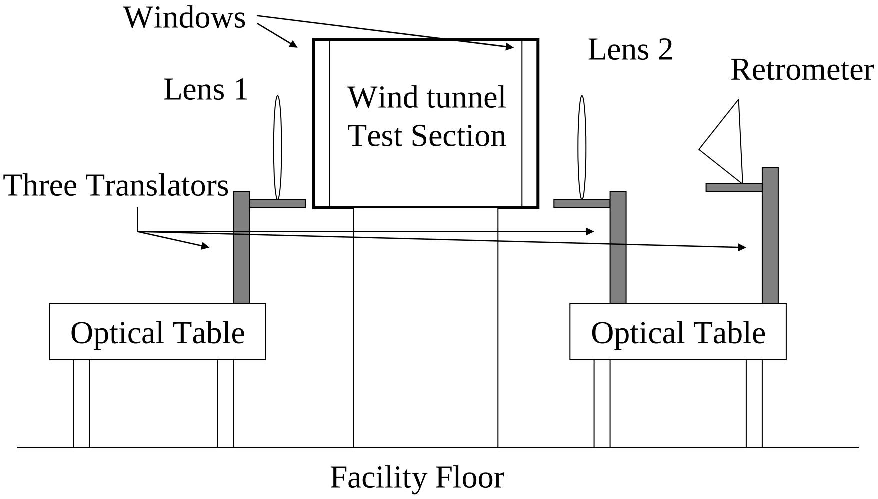

Fig. 5b End-view schematics of SRGS apparatus at the UPWT.

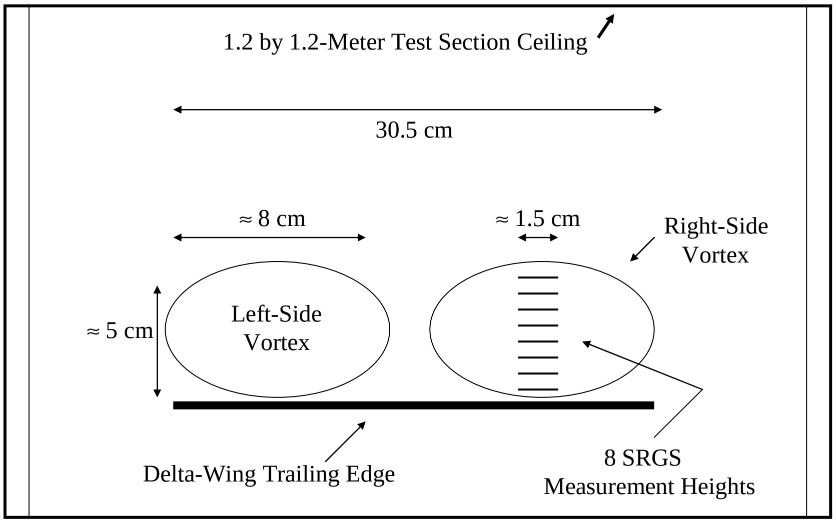

Fig. 5c Magnified end-view schematic illustrating (not to scale) cross sections of twin streamwise vortices and the SRGS sample volume size, shape, and eight vertical heights.

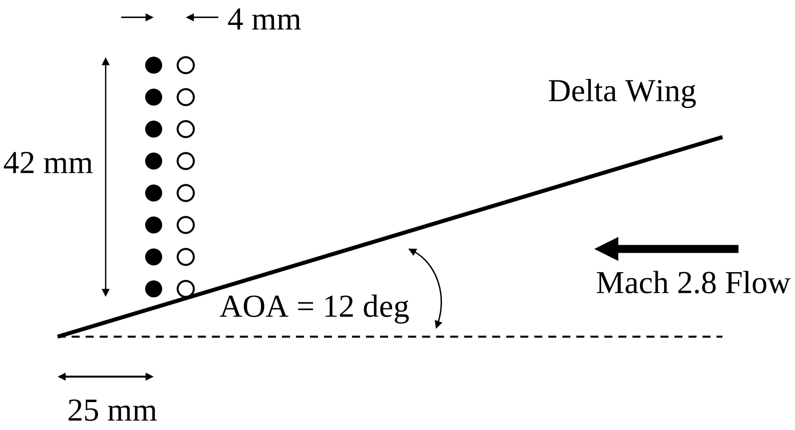

Fig. 5d Magnified side-view schematic illustrating (not to scale) cross sections of twin streamwise vortices and the SRGS sample volume size, shape, and sixteen locations.

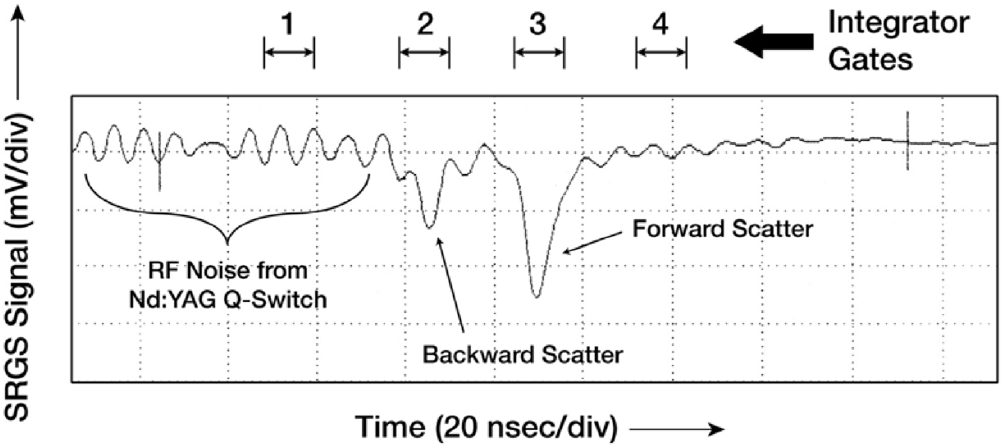

Fig. 6 Example of temporal structure of forward and backward Raman signals for a single laser pulse, at 100 kPa (1 atm), 300 K, and 35 mJ of energy in the 10-nsec pump pulse. Gates 2 and 3 capture the two signals, while gates 1 and 4 capture nearly simultaneous backgrounds that record a low-frequency (~ 1 MHz) noise (not obvious in the short 200-nsec duration in this figure) that can be subtracted from the signals on an every-pulse basis.

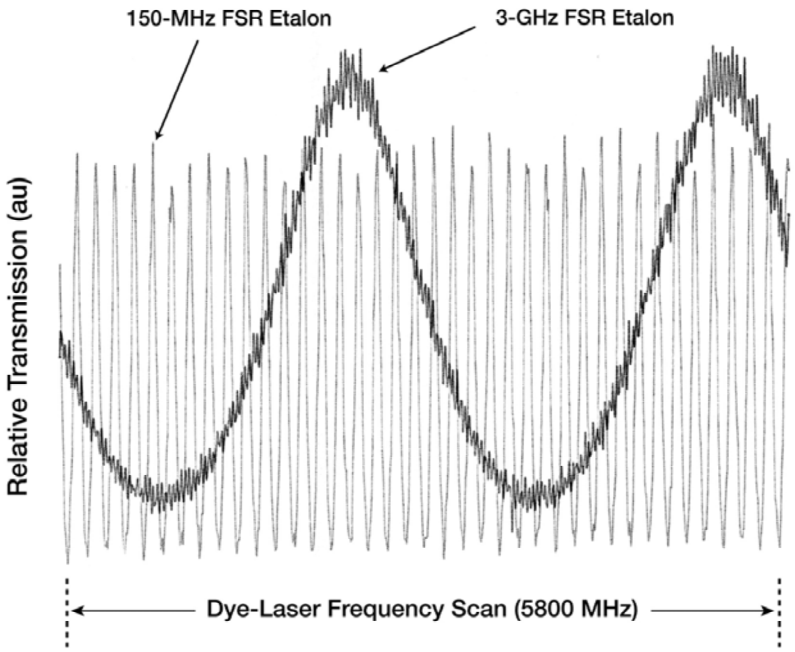

Fig. 7 Transmission curves of dye-laser diagnostic beams through 150-MHz and 3-GHz FSR etalons, for a single 5800-MHz dye-laser wavelength scan.

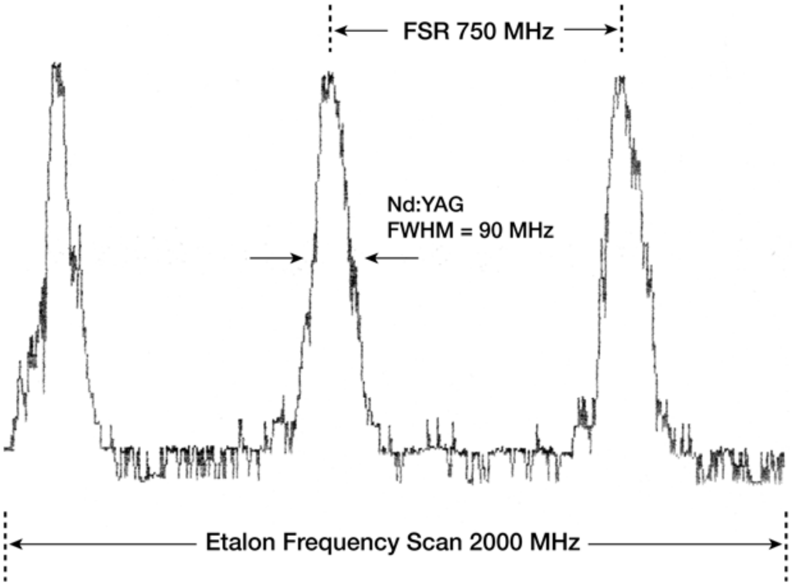

Fig. 8 Measurement of the averaged linewidth of the single-frequency Nd:YAG laser (532 nm) acquired during a single 60-sec dye-laser wavelength scan. The frequency scale on the abscissa corresponds to Nd:YAG frequency, not dye-laser frequency.

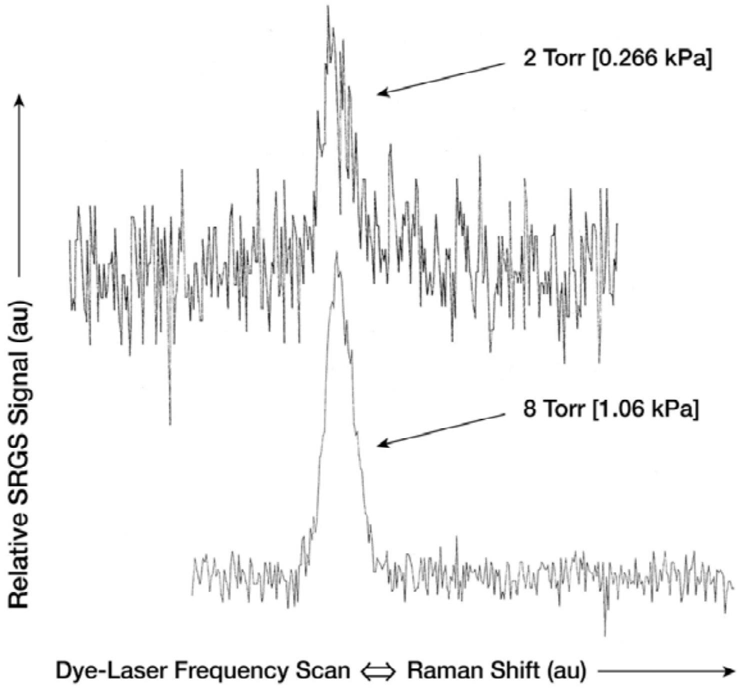

Fig. 9a Wavelength scans (60 sec) over the J = 12 Q-branch transition for 2 and 8 Torr at temperature 295 K and with pump energy/pulse of 145 mJ/pulse.

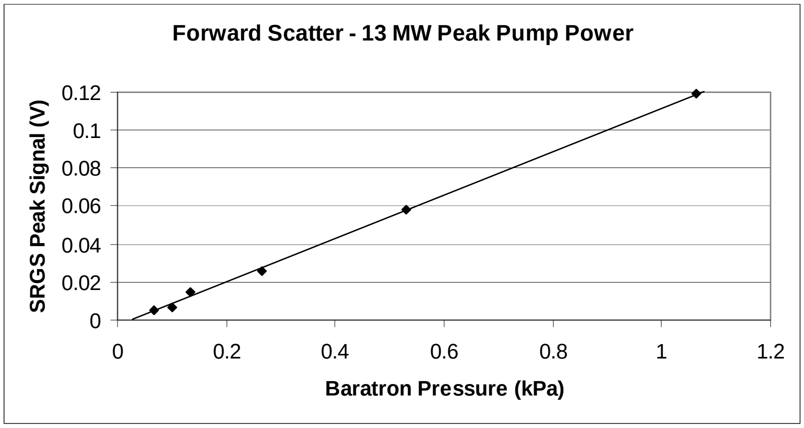

Fig. 9b Pressure dependence of the peak SRGS signal strength (J = 12) as a function of gas pressure (temperature = 295 K). The line is a fit by eye.

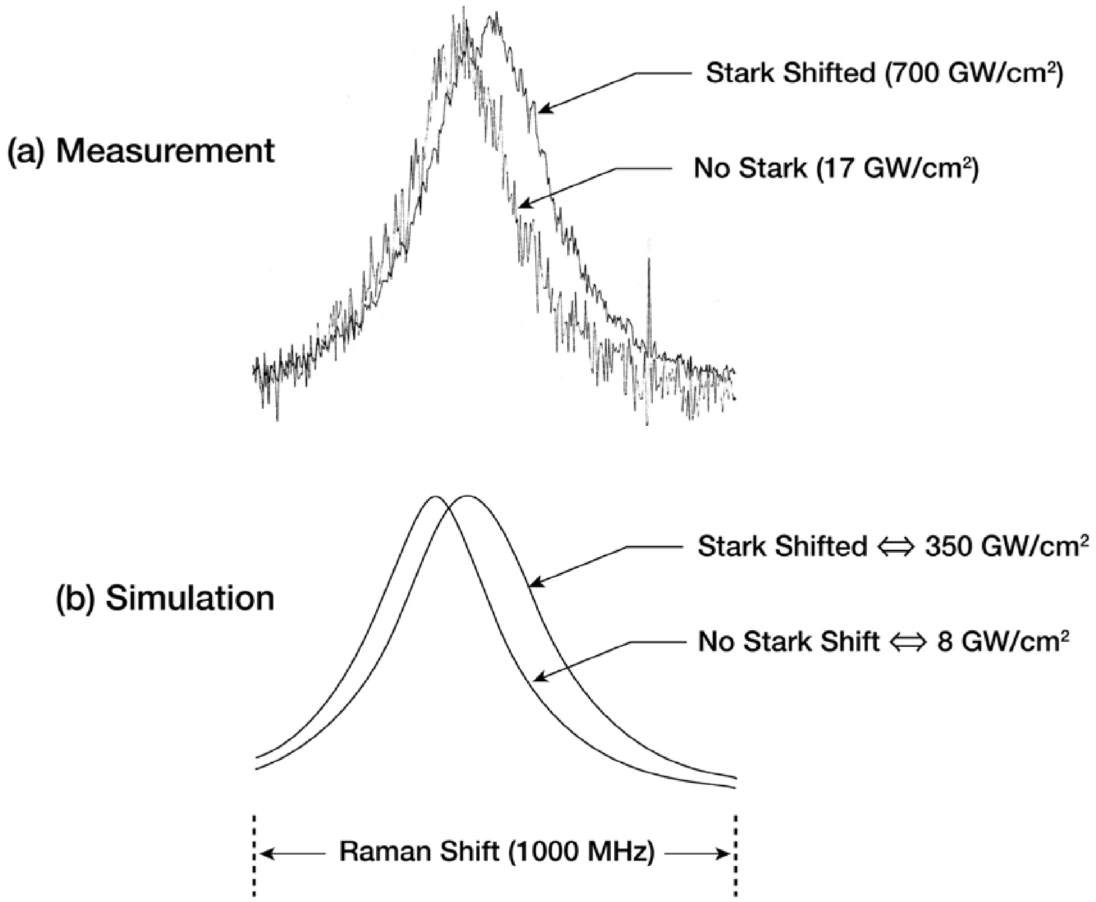

Fig. 10 Stark broadening (a) measurements for no-Stark (i.e., small laser peak power of ~ 17 GW/cm^2), and Stark-broadened (large peak power ~ 700 GW/cm^2 measured peak intensity) line shapes with beams crossed at 0.9 deg. The (b) numerically simulated intensity that best fits the data is 350 GW/cm^2. Gas sample is pure N_2 at 300 K and 1 atm.

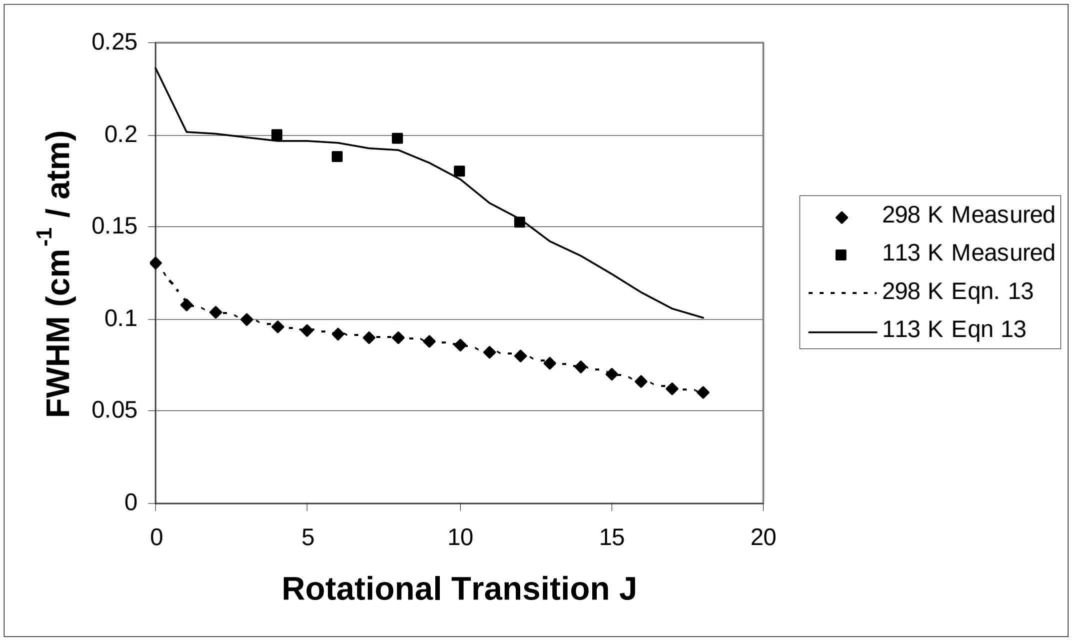

Fig. 11 N_2 vibrational Q-branch collisional broadening coefficients. This is a comparison of the J dependence of the empirical pressure broadening coefficients from Eq. 13 (solid and dashed lines) and data from Ref. 28 (symbols) for two temperatures (298 K for bottom curve and 113 K for top curve).

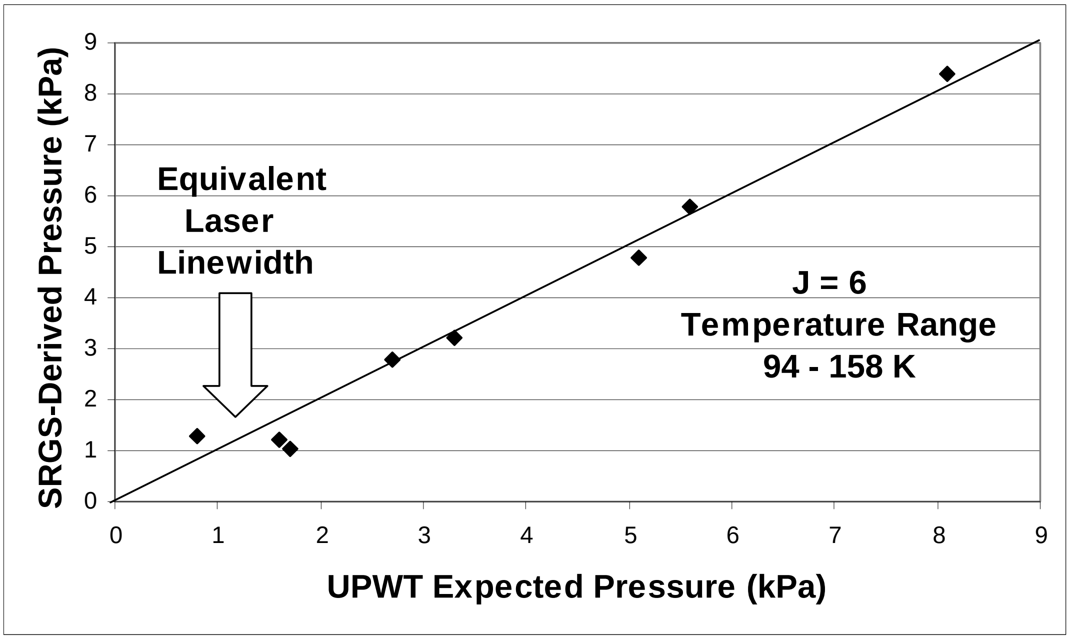

Fig. 12 Comparison of UPWT free-stream pressure from traditional UPWT instrumentation and SRGS line-shape measurements using the pressure broadening coefficients from Ref. 28. The good agreement of these two data sets is an independent confirmation of the low-temperature pressure broadening measurements of Ref. 28.

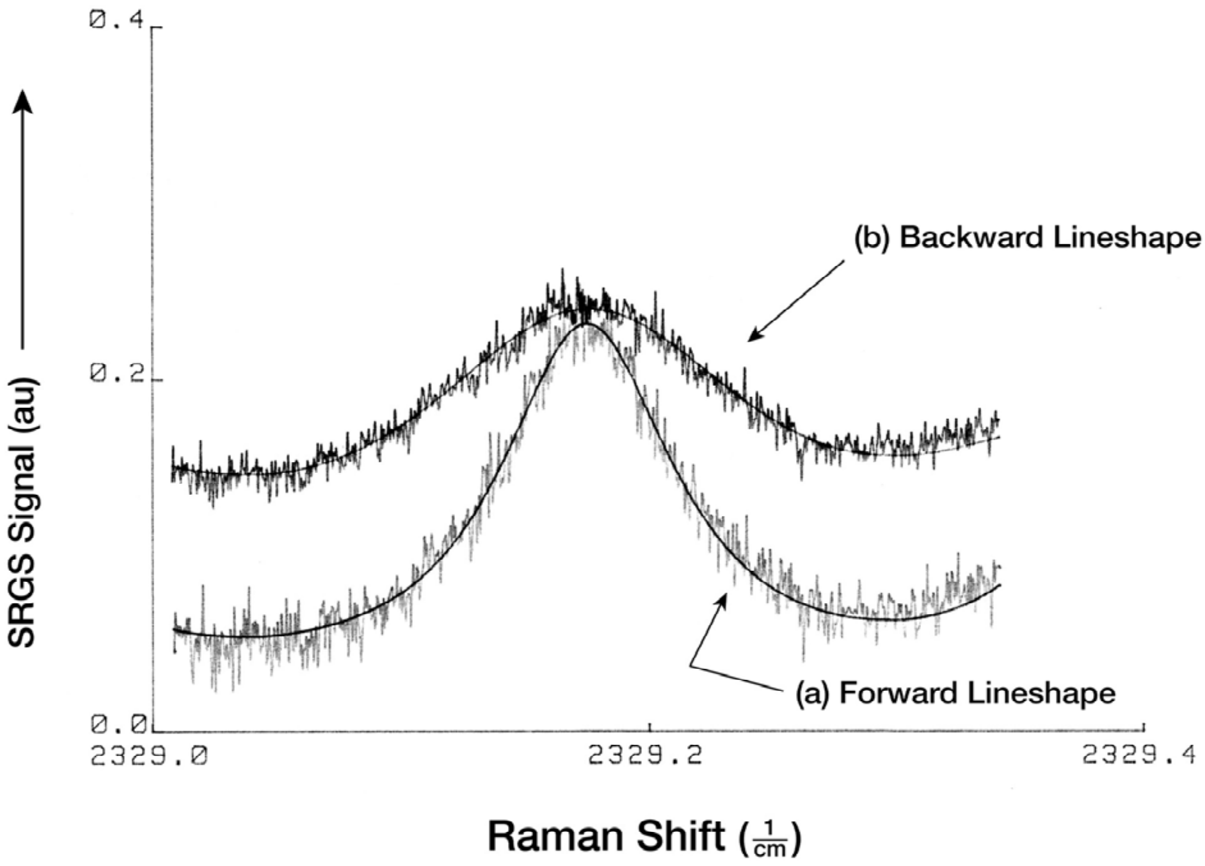

Fig. 13 Example of data of a single 30-sec scan over the J = 6 transition, at 1 atm and 300 K (noisy profiles), and Voigt fits (smooth curves) that show (a) forward and (b) backward Raman line shapes for no flow, after subtraction.

Laboratory and UPWT data on still air

All points are single 30-sec measurements, except one square point for pressure

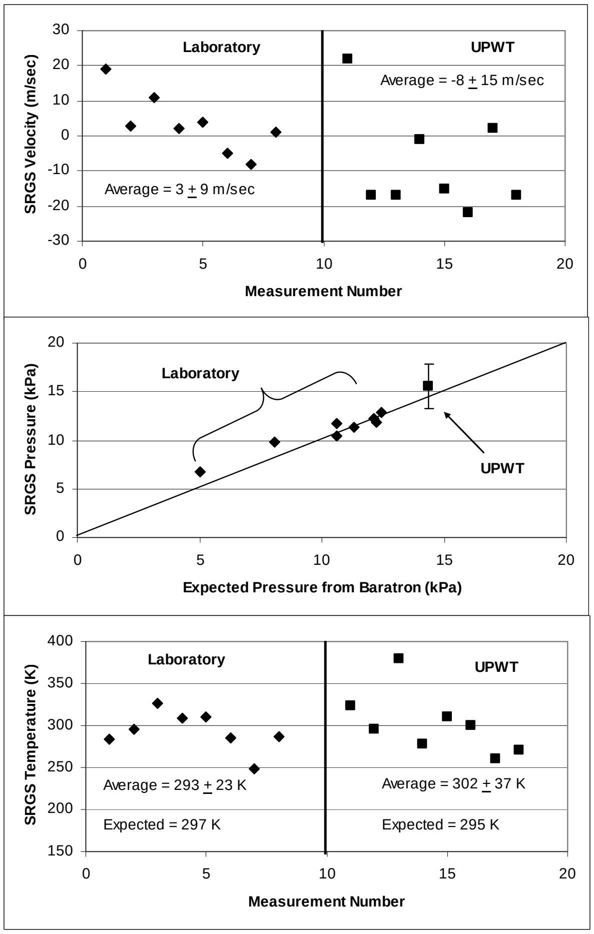

rms deviation: ± 13 m/sec

rms deviation: ± 1.0 kPa

rms deviation: ± 17 K

Fig. 14 No-flow measurements of velocity, pressure, and temperature from a laboratory cell containing N_2 at room temperature (left side) and in air at the UPWT test section with no flow (right side). The average pressure corresponding to all UPWT velocity data is shown as the square data point with the error bar in the pressure plot.

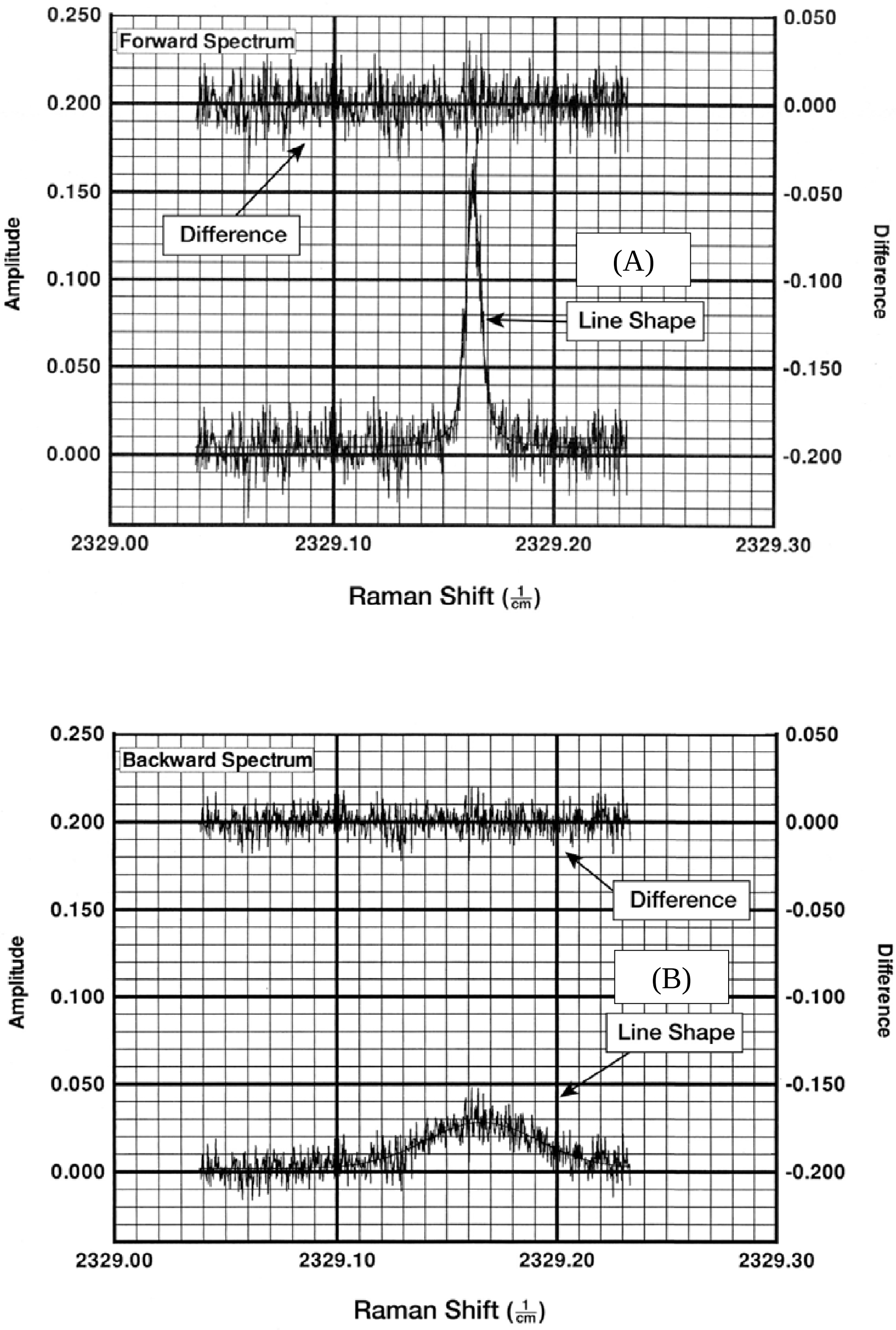

Fig. 15 Single 30-sec scan, over the J = 6, in the free stream (Mach 2.3, static pressure 2.4 kPa (0.024 atm), and temperature 158 K) that shows (a) forward and (b) backward line shapes, after subtraction. The smooth curve through each noisy line shape is a Voigt fit to the data. Above each line shape, the difference between the data and fit is also plotted versus scan frequency.

UPWT free-stream results

Each point is an average of 3-8 (30-sec) scans

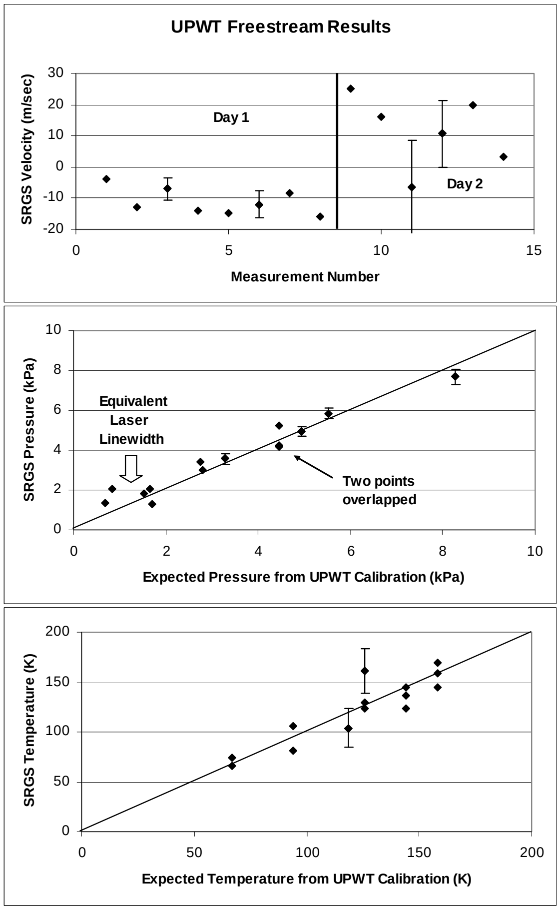

rms deviation: ± 14 m/sec

rms deviation: ± 0.4 kPa

rms deviation: ± 14 K

Fig. 16 Comparison of SRGS-derived values and expected free-stream tunnel conditions for cross-flow velocity, pressure, and temperature.

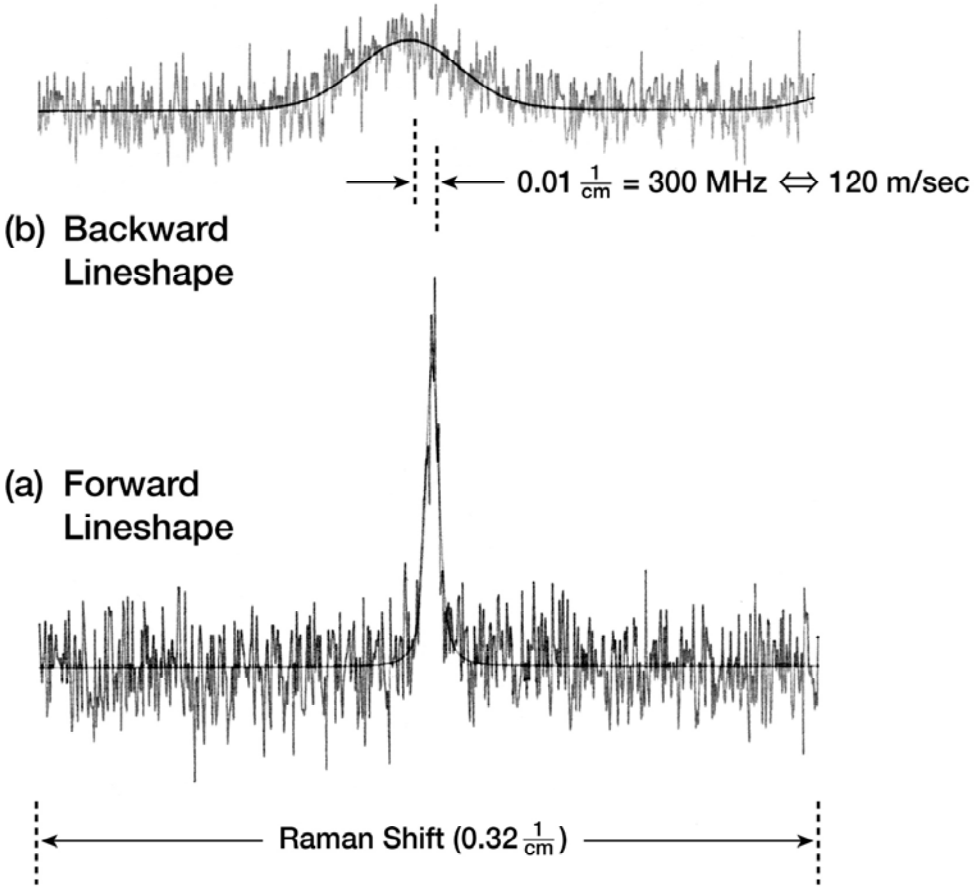

Fig. 17 Example of single 30-sec scan at the 40-mm location (above the model surface) of the vortex showing (a) forward and (b) backward line shapes and fits, after subtraction. The smooth curve through each noisy line shape is a Voigt fit. The shift between the forward and backward line centers corresponds to about 120 m/sec.

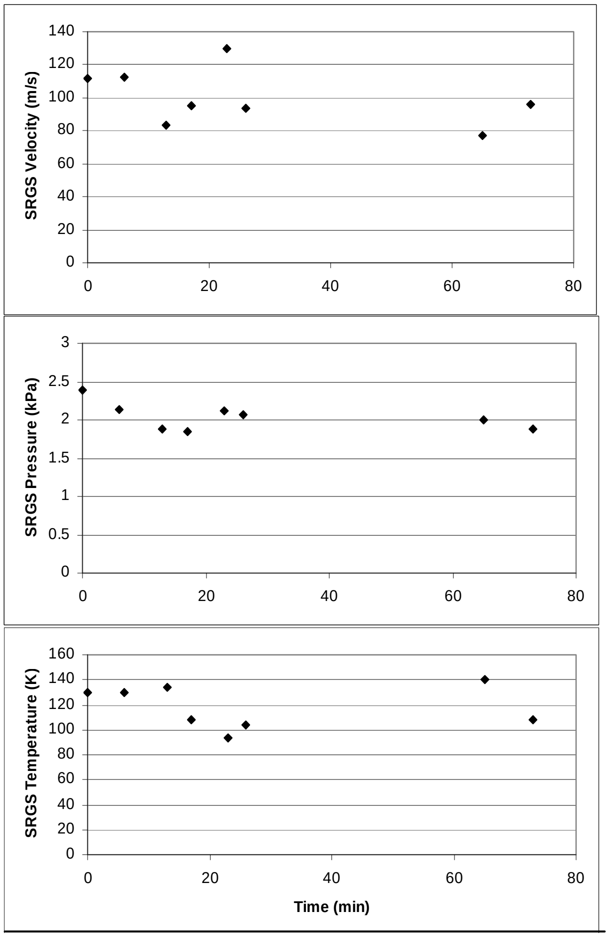

Fluctuations at one vortex location (4 cm above surface)

1 σ of mean: ± 6 m/sec

1 σ of mean: ± 0.06 kPa

All points are 30-sec single-scan measurements

1 σ of mean: ± 6 K

Fig. 18 Series of single 30-sec measurements, at one off-center position in the vortex core for simultaneous velocity, pressure, and temperature versus time.

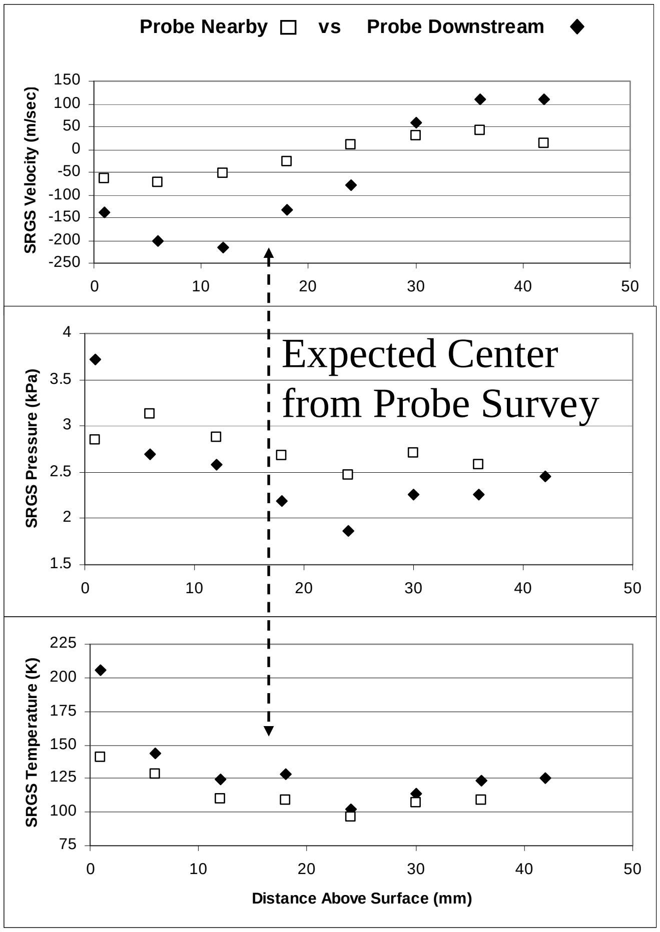

Vertical scan through center of vortex core

All points are averaged over ≈ six 30-sec scans / point, requiring ≈15 min

1 σ of mean:
± 10 m/sec

1 σ of mean:
± 0.1 kPa

1 σ of mean:
± 10 K

Fig. 19 SRGS measurement of flow parameters 25 mm upstream of the trailing edge of a delta wing (over a line extending vertically above surface and through a vortex core). Solid diamonds show a profile with the Pitot probe backed well downstream of the trailing edge, and open squares show a second profile taken 29 mm upstream from the trailing edge and with the Pitot probe positioned with its front tip ≈ 5 mm downstream of the SRGS sample volume. The dashed double-headed arrow shows the expected center location from the pitot probe survey.

REPORT DOCUMENTATION PAGE

Form Approved
OMB No. 0704-0188

1. REPORT DATE *(DD-MM-YYYY)*
01- 10 - 2008

2. REPORT TYPE
Technical Memorandum

3. DATES COVERED *(From - To)*

4. TITLE AND SUBTITLE
Measurement of Off-Body Velocity, Pressure, and Temperature in an Unseeded Supersonic Air Vortex by Stimulated Raman Scattering

5a. CONTRACT NUMBER

5b. GRANT NUMBER

5c. PROGRAM ELEMENT NUMBER

6. AUTHOR(S)
Herring, Gregory C.

5d. PROJECT NUMBER

5e. TASK NUMBER

5f. WORK UNIT NUMBER
984754.02.07.07.21.33

7. PERFORMING ORGANIZATION NAME(S) AND ADDRESS(ES)
NASA Langley Research Center
Hampton, VA 23681-2199

8. PERFORMING ORGANIZATION REPORT NUMBER
L-19545

9. SPONSORING/MONITORING AGENCY NAME(S) AND ADDRESS(ES)
National Aeronautics and Space Administration
Washington, DC 20546-0001

10. SPONSOR/MONITOR'S ACRONYM(S)
NASA

11. SPONSOR/MONITOR'S REPORT NUMBER(S)
NASA/TM-2008-215535

12. DISTRIBUTION/AVAILABILITY STATEMENT
Unclassified - Unlimited
Subject Category 74
Availability: NASA CASI (301) 621-0390

13. SUPPLEMENTARY NOTES
An electronic version can be found at http://ntrs.nasa.gov

14. ABSTRACT

A noninvasive optical method is used to make time-averaged (30 sec) off-body measurements in a supersonic airflow. Seeding of tracer particles is not required. One spatial component of velocity, static pressure, and static temperature are measured with stimulated Raman scattering. The three flow parameters are determined simultaneously from a common sample volume (0.3 by 0.3 by 15 mm) using concurrent measurements of the forward and backward scattered line shapes of a N2 vibrational Raman transition. The capability of this technique is illustrated with laboratory and large-scale wind tunnel testing that demonstrate 5-10% measurement uncertainties. Because the spatial resolution of the present work was improved to 1.5 cm (compared to 20 cm in previous work), it was possible to demonstrate a modest one-dimensional profiling of cross-flow velocity, pressure, and translational temperature through the low-density core of a stream-wise vortex (delta-wing model at Mach 2.8 in NASA Langley's Unitary Plan Wind Tunnel).

15. SUBJECT TERMS
Velocimetry; Thermometry; Pressure measurement; Stimulated Rman spectroscopy; Supersonic delta-wing vortex

16. SECURITY CLASSIFICATION OF:			17. LIMITATION OF ABSTRACT	18. NUMBER OF PAGES	19a. NAME OF RESPONSIBLE PERSON
a. REPORT	b. ABSTRACT	c. THIS PAGE			STI Help Desk (email: help@sti.nasa.gov)
					19b. TELEPHONE NUMBER *(Include area code)*
U	U	U	UU	49	(301) 621-0390